

Uncertainty quantification for White Matter Hyperintensity segmentation detects silent failures and improves automated Fazekas quantification

Ben Philips^{a,*}, Maria del C. Valdes Hernandez^b, Chen Qin^c, Una Clancy^b, Eleni Sakka^b, Susana Munoz Maniega^b, Mark E. Bastin^b, Angela C.C. Jochems^b, Joanna M. Wardlaw^b, Miguel O. Bernabeu^d, Alzheimer's Disease Neuroimaging Initiative (ADNI)¹

^a*School of Informatics, University of Edinburgh, Edinburgh EH8 9AB, United Kingdom*

^b*Centre for Clinical Brain Sciences, Chancellor's Building, University of Edinburgh, Edinburgh EH16 4SB United Kingdom*

^c*Department of Electrical and Electronic Engineering & I-X, Imperial College London, London SW7 2AZ, United Kingdom*

^d*Centre for Medical Informatics, Usher Institute, University of Edinburgh, Edinburgh EH16 4UX, United Kingdom*

Abstract

White Matter Hyperintensities (WMH) are key neuroradiological markers of small vessel disease present in brain MRI. Assessment of WMH is important in research and clinics. However, WMH are challenging to segment due to their high variability in shape, location, size, poorly defined borders, and similar intensity profile to other pathologies (e.g stroke lesions) and artefacts (e.g head motion). In this work, we apply the most effective techniques for uncertainty quantification (UQ) in segmentation to the WMH segmentation task across multiple test-time data distributions. We find a combination of Stochastic Segmentation Networks with Deep Ensembles yields the highest Dice and lowest Absolute Volume Difference % (AVD) score on in-domain and out-of-distribution data. We demonstrate the downstream utility of UQ, proposing a novel method for classification of the clinical Fazekas score using spatial features extracted for WMH segmentation and UQ maps. We show that incorporating WMH uncertainty information improves Fazekas classification performance and calibration, with median class balanced accuracy for classification models with (UQ and spatial WMH features)/(spatial WMH features)/(WMH volume only) of 0.71/0.66/0.60 in the Deep WMH and 0.82/0.77/0.73 in the Periventricular WMH regions respectively. We demonstrate that stochastic UQ techniques with high sample diversity can improve the detection of poor quality segmentations. Finally, we qualitatively analyse the semantic information captured by UQ techniques and demonstrate that uncertainty can highlight areas where there is ambiguity between WMH and stroke lesions, while identifying clusters of small WMH in deep white matter unsegmented by the model.

Keywords: Uncertainty Quantification, White Matter Hyperintensities, Fazekas Prediction, Machine Learning, Brain MRI

1. Introduction

Cerebral small vessel disease (SVD) is a significant vascular contributor to stroke, cognitive decline, and dementia. One of its main neuroradiological signatures are White Matter Hyperintensities (WMH). They reflect brain tissue damage ranging from altered interstitial fluid mobility and water content to demyelination and axonal loss (Wardlaw et al., 2015), and appear as clusters with increased signal in the T2-weighted-based sequences from brain magnetic resonance imaging (MRI) scans, typically increasing in incidence with age. WMH foci are indicative

of more widespread and subtle changes (Maillard et al., 2011), (Valdés Hernández et al., 2014) and a predictor for increased stroke and mortality risks (DeBette and Markus, 2010). Depending on brain location, WMH may have differing etiological substrates Kim et al. (2008) and correlates Wang et al. (2022); Jiménez-Balado et al. (2022); Gootjes et al. (2004); Griffanti et al. Hence, assessment of WMH burden, location, and correlation with clinical outcomes is important in clinical trials and epidemiological studies.

WMH burden in scans of elderly and SVD patients is typically visually assessed by neuroradiologists separately in the periventricular and deep white matter regions using Fazekas scores (Fazekas et al., 1987). However, despite the straightforwardness of this visual rating scale, reliable assessment of WMH requires substantial expertise due to their heterogeneity in presentation and often simultaneous presence and sometimes coalescence of other pathologies of similar signal intensity characteristics (Ding et al.). The gold standard for WMH computational assess-

*Corresponding author

Email address: B.R.Philips@sms.ed.ac.uk (Ben Philips)

¹This article uses data obtained from the Alzheimer's Disease Neuroimaging Initiative (ADNI) database (adni.loni.usc.edu). As such, the investigators within the ADNI contributed to the design and implementation of ADNI and/or provided data but did not participate in analysis or writing of this report. A complete listing of ADNI investigators can be found at: http://adni.loni.usc.edu/wp-content/uploads/how_to_apply/ADNI_Acknowledgement_List.pdf

ment is manual delineation in fluid-attenuated inversion recovery (FLAIR) MRI. However, manual annotation of WMH is time-consuming, subject to inter-rater variability and requires substantial training time, as the boundaries between normal appearing white matter and the hyperintense tissue are generally ill-defined and difficult to delineate. Moreover, given the co-existence of WMH with features of similar appearance or even imaging artefacts, the identification of deep isolated WMH is sometimes subjective. These imply the existence of a distribution of multiple potential WMH segmentations and, by extension, Fazekas scores. Hence fast and reliable probabilistic automated techniques for WMH segmentation are essential.

Artificial Intelligence (AI) techniques have shown broad applicability to clinical (Monsour et al., 2022; Barnett et al.) and research goals (Nenning and Langs, 2022) across a wide range of neuroimaging settings (Choi and Sunwoo, 2022) and disease types (Leming et al., 2023; Ruffle et al., 2023). In recent years a number of approaches have been developed to segment WMH lesions automatically with promising results (Balakrishnan et al., 2021). In particular, Convolutional Neural networks (CNNs) have yielded unprecedented performance (Litjens et al., 2017) in this segmentation task (Park et al., 2021; Mojiri Forooshani et al.; Guerrero et al.; Rachmadi et al., 2020; Zhao et al., 2021; Joo et al., 2022).

However, as most AI schemes, such techniques face reliability and robustness concerns that still hamper their trust and deployment (Cuttillo et al., 2020), (Zou et al., 2023a), (Lim et al., 2019), particularly in the face of limited, biased or unrepresentative data sources. Large, population scale analysis of treatment effects and disease progression will likely increasingly rely on access to data collected across a multitude of scanning sites with accompanying variations in acquisition protocol (Borchert et al.; Van Horn and Toga, 2014), or clinical imaging data (Ruffle et al., 2023; Gao et al.) where image quality is typically lower. But while such data allows detecting complex patterns, this diversity in input covariates introduces clear robustness challenges for our models. Consequently, researchers and clinicians may wish to avoid delegating decision making to AI tools (Begoli et al., 2019), or to avoid AI generated information entirely when making decisions. Thus it is desirable to implement models that are not only robust but can quantify any uncertainties in the inferences made. Uncertainty quantification (UQ) is often touted as essential (Begoli et al., 2019) and a core tenement of improving the trust of such systems (Zou et al., 2023b). In the context of segmentation, this may be represented as a separate UQ output or a distribution of possible segmentations. This uncertainty should ideally reliably provide information on where a segmentation may be incorrect or the image is ambiguous (Czolbe et al., 2021), and estimate the true frequency of different spatially variant segmentations (Monteiro et al., 2020; Kohl et al., 2018).

UQ has been applied across a wide range of medical tasks (Yeung et al., 2023; Abdar et al.; Oda et al., 2021;

Tanno et al., 2021), imaging modalities (Lambert et al., 2024; Joy et al., 2021; Yeung et al., 2023) and data challenges from incomplete data to measurement variability (Seoni et al., 2023) and image denoising (Laves et al., 2020). UQ techniques typically modify our existing neural network models to produce a calibrated confidence evaluation along with the prediction of the segmentation model. They are commonly used for improving the quality of the predictions at inference time (You et al., 2023; S and Fleuret; Rahman et al.; Zou et al., 2023b), such as uncertainty aware aggregation of predictions at different scales, improving segmentation when the target objects vary significantly in size and intensity (Oda et al., 2021), or to prevent overfitting to image noise in Bayesian deep image prior networks (Laves et al., 2020). For WMH segmentation, UQ could inform on ambiguous regions or model failures, capture unusual pathologies and generate multiple plausible segmentation possibilities. This improves the reliability of such models while effectively estimating the confidence of their outputs. Using uncertainty features for quality control has proved effective in various areas (Joy et al., 2021), with aleatoric uncertainty predicting segmentation error (Czolbe et al., 2021), or detecting poor quality predictions (Liang et al., 2022). More generally, as increasing interest in deploying neural networks in high risk scenarios increases, so does the importance of ensuring the trustworthiness of our models (Li et al., 2023a).

While many works have assessed UQ techniques, a comparison of the utility of different techniques for *downstream* clinical tasks is lacking (Czolbe et al., 2021; Zou et al., 2023a). In this work we compare multiple UQ techniques not only in terms of their visual utility in WMH assessment, but propose that UQ information can be used to enhance the prediction of the downstream clinical Fazekas score and for assessing the quality (e.g Dice score) of the WMH segmentations. We perform both these downstream tasks by extracting volumetric and spatial features from the UQ representations and WMH segmentations as inputs to a classifier.

In this work, we present 4 main contributions. First, we benchmark UQ methods for WMH segmentation and analyse the robustness and uncertainty map utility on in-distribution and real world out-of-distribution data. We explore the Softmax entropy, MonteCarlo Dropout, Deep Ensembles, Evidential Deep learning, Explicit Heteroscedastic Classification (including Stochastic Segmentation Networks), and Probabilistic U-Net, and demonstrate the robustness gains of modelling both epistemic and aleatoric uncertainty. Secondly, we propose a novel method for Fazekas classification using spatial features extracted for WMH segmentation maps, and investigate how UQ map information can improve the prediction of the Fazekas score. Thirdly, we explore whether UQ features can aid in the identification of low quality segmentations, and finally we provide a qualitative analysis of the semantic information contained in UQ maps.

2. Background

2.1. Uncertainty quantification overview

Uncertainty can be split into two types: epistemic (model uncertainty) and aleatoric (data uncertainty) (Abdar et al.; Wimmer et al., 2023). Epistemic uncertainty reflects a lack of knowledge about the input, which is high for out-of-distribution (OOD) and unseen data and can thus be reduced with more data. In our case, epistemic uncertainty includes changes in MRI acquisition characteristics and differences in train and test subject cohort demographics. Aleatoric uncertainty captures the inherently irreducible uncertainty found in the data (i.e the set of possible outputs for a given input implied by the data (Abdar et al.)). In our case, the boundary of WMH within the WMH "penumbra", the possible misclassified foci due to inter-observer differences, coexistence of WMH with other similar pathologies, or confounding imaging artefacts may be sources of aleatoric uncertainty.

2.2. Uncertainty quantification techniques

In this section we outline the task at hand and then draw out the principles behind the core types of UQ techniques bench-marked in this work. Given a dataset $\mathcal{D} = \{\mathbf{x}^{(n)}, \mathbf{y}^{(n)}\}_{n=1}^N$ of brain MRI images \mathbf{x} and segmentation labels \mathbf{y} , where \mathbf{x} is a pair of FLAIR and T1-weighted images and \mathbf{y} is a voxelwise binary segmentation mask, our task is to construct a model $f(\mathbf{x})$ with learned parameters θ that predicts $p(\mathbf{y}|\mathbf{x}, \mathcal{D}; \theta)$. For the purposes of training our model, we consider x and y to refer to individual 2D axial slices of brain MRI images. For our evaluation we will combine the predictions across all slices of an individual to perform 3D analysis of our models (see section).

2.2.1. Softmax Entropy

Softmax entropy is a very simple and commonly employed technique that utilises the entropy of the Softmax distribution $\mathcal{H}[p(\mathbf{y}|\mathbf{x}, \mathcal{D}; \theta)]$, and requires no architectural modifications to a typical neural network (e.g U-Net), with no extra computational overhead. Softmax Entropy provides an effective representation of aleatoric uncertainty for in distribution data (Mukhoti et al., 2021b). However it is essential to employ a loss function that rewards a calibrated model (e.g by utilising a proper scoring loss function such as cross entropy).

2.2.2. Monte-Carlo dropout

Bayesian neural networks provide a principled approach to model epistemic uncertainty, by representing the model weights as a probability distribution. However computing the posterior predictive distribution analytically is intractable for the neural networks we typically use for segmentation. Hence, multiple approaches for approximating the posterior probability distribution have been proposed (Blei et al., 2017), (Blundell et al., 2015), (Gal and Ghahramani, 2016) (D'Angelo et al., 2021) which re-frame Bayesian inference as an optimization problem.

Monte-Carlo dropout (MC-Dropout) (Gal and Ghahramani, 2016) is a quasi variational inference technique that utilises dropout (Srivastava et al., 2014) at test time to generate stochastic passes through the model and heavily used in the UQ literature. MC-Dropout approximates the Bayesian posterior predictive as:

$$p(\mathbf{y}|\mathbf{x}, \mathcal{D}) \approx \frac{1}{S} \sum_{s=1}^S p(\mathbf{y}|\mathbf{x}, \theta^{(s)}), \quad (1)$$

where $\theta^{(s)} \sim p(\theta|\mathcal{D})$. However this term is intractable, so it is approximated as $\theta^{(s)} = \theta \odot z^{(s)}$, where $z^{(s)}$ is a randomly generated binary dropout mask. MC Dropout has been utilised across the medical imaging literature (Lambert et al., 2024; Hu et al., 2019; Hellström et al., 2023; Laves et al., 2020), and has been used in WMH segmentation to improve robustness to downsampling and gamma correction augmentations intended to replicate possible perturbations found in clinical data (Mojiri Forooshani et al.).

2.2.3. Deep Ensembles

Deep Ensembles are a simple technique (Lakshminarayanan et al., 2017) that are typically state-of-the-art for UQ (Abdar et al.). Deep Ensembles involves training multiple models (elements). There are a broad range of ensembling strategies (Ganaie et al., 2022). Here we focus on a simple deep ensemble strategy where multiple instances of the same base model are trained with different random weight initializations, with a different random shuffling order per model of the training dataset for each epoch. This strategy relies on the non convex behaviour of the loss surface and the stochasticity of the optimization process (Abe et al., 2022) to achieve a set of diverse models which collectively outperform individual elements of the ensemble (Lee et al., 2015), and have improved performance in WMH segmentation (Guo et al. (2022); Molchanova et al. (2025)). Ensembles can provide well calibrated predictions (Lakshminarayanan et al., 2017) and show robustness to shifts in the input data distribution (Ovadia et al., 2019), (Mehrtens et al., 2022). The results from each model can be treated as samples from an aggregate model, from which we acquire a sample distribution in terms of volumes and spatial coverage, that approximates the Bayesian posterior predictive distribution as a uniform mixture of delta distributions centered at the weight vector of each ensemble component.

2.2.4. Evidential Deep Learning

Bayesian approaches to uncertainty do not quantify the predictive uncertainty directly, but focus on the uncertainty of the model weights. Some approaches, concerned with the efficiency of generating uncertainty estimates, use 'single pass' methods that do not require any form of sampling. Single pass methods generally fall into two categories: Bayesian Last Layer techniques (Harrison et al., 2024) and Evidential Deep Learning (Han et al., 2022),

(Sensoy et al., 2018) or distance-based methods (Liu et al., 2023), (Mukhoti et al., 2023), (Mukhoti et al., 2021a).

While distance-based techniques typically rely on special regularization of the model layers, such as spectral normalization, evidential deep learning makes no modification to the underlying network architecture.

Evidential Deep Learning techniques (Ulmer, 2021) model the predictive uncertainty by placing a prior distribution directly over the likelihood function. In the classification setting, we can do this by placing a Dirichlet distribution over the parameters of the categorical distribution typically output from the Softmax layer of a neural network. The resulting posterior distribution gives us a second order probability distribution over possible Softmax outputs for each input, inherently able to represent both epistemic and aleatoric uncertainty. While multiple formulations of Evidential DL exist, here we follow a framework that directly parameterizes this posterior distribution, which has previously been applied to medical imaging segmentation tasks producing well calibrated models with robustness to adversarial inputs (Zou et al., 2022; Li et al., 2023b). Here the model provides pseudo-counts e_c (evidence) for each class (i.e WMH or not for a particular voxel) with which we update a uniform Dirichlet prior (i.e $\alpha = \mathbf{1}$ for Dirichlet concentration parameters α). To do this we define the posterior concentration parameters β as $\beta_c = (e_c + 1)^2$ following (Li et al., 2023b). To ensure a valid probability distribution, e is constrained to be positive with a Softplus layer. Evidential DL can be extended to segmentation by predicting one Dirichlet distribution per voxel in the output. From now on, we refer to the evidence for all voxels as \mathbf{e} where \mathbf{e}_{vc} is the evidence for voxel v and class c , with an analogous annotation for posterior Dirichlet parameters β and sampled categorical distributions \mathbf{p} .

To optimize the model, we calculate the Bayes risk of an objective function of our choosing (the expected value of our cost function over all possible settings of \mathbf{p}_v for each voxel v).

The corresponding Bayes risk for the cross entropy loss can be shown to equal the following (Sensoy et al., 2018):

$$\mathcal{L}_{\text{evid_xent}} = \frac{1}{V} \sum_{v=1}^V \sum_{c=1}^C \mathbf{y}_{vc} (\psi(\mathbf{S}_v) - \psi(\alpha_{vc})), \quad (2)$$

where \mathbf{S}_v is the Dirichlet strength for voxel v , $\mathbf{S}_v = \sum_c^C (\mathbf{e}_{vc} + 1)^2$ where $\psi(x) = \frac{d}{dx} \log \Gamma(x)$ is the digamma function. The bayes risk for the soft Dice loss is equivalent to the following (Li et al., 2023b):

$$\mathcal{L}_{\text{evid_sDice}} = 1 - \frac{2}{C} \sum_{c=1}^C \frac{\sum_v \mathbf{y}_{vc} \frac{\alpha_{vc}}{\mathbf{S}_v}}{\sum_v \left(\mathbf{y}_{vc}^2 + \left(\frac{\alpha_{vc}}{\mathbf{S}_v} \right)^2 + \frac{\alpha_{vc}(\mathbf{S}_v - \alpha_{vc})}{\mathbf{S}_v^2(\mathbf{S}_v + 1)} \right)}. \quad (3)$$

However, in order to ensure that the model is effective in representing the epistemic uncertainty in unknown inputs (i.e by providing less evidence for incorrect labels and

OOD inputs generally) the model must be regularized. Ulmer et al. we follow the typical approach of adding a Kullback-Leibler (KL) divergence term between the predicted Dirchlet distribution for each voxel and the uniform Dirchlet distribution Zou et al. (2022). We do this only for incorrectly classified voxels. The KL divergence, averaged over all voxels is given as:

$$\mathcal{L}_{\text{evid_KL}} = \sum_{v=1}^V \left(\log \left(\frac{\Gamma \left(\sum_{c=1}^C \tilde{\alpha}_{vc} \right)}{\Gamma(C) \prod_{c=1}^C \Gamma(\tilde{\alpha}_{vc})} \right) + \left(\sum_{c=1}^C (\tilde{\alpha}_{vc} - 1) \right) \left[\psi(\tilde{\alpha}_{vc}) - \psi \left(\sum_{c'=1}^C \tilde{\alpha}_{vc'} \right) \right] \right), \quad (4)$$

where $\tilde{\alpha}_{vc} = \mathbf{y}_{vc} + (1 - \mathbf{y}_{vc}) \odot \alpha_{vc}$ is used to mask out correct predictions (i.e to ensure that only misleading evidence is penalized).

To classify a given voxel v we first sample a categorical distribution from a Dirchlet with parameters β_v . Finally, the predicted class probabilities are given by:

$$\frac{\beta_v}{\mathbf{S}_v} \quad (5)$$

2.2.5. Explicit Heteroscedastic Classification and Stochastic Segmentation Networks

An alternative approach to explicitly modelling the aleatoric uncertainty is to learn a distribution over model output logits. In explicit heteroscedastic classification, the logits $\boldsymbol{\eta}_v$ for each voxel v are assumed to be a Gaussian with mean $\mu(\mathbf{x}_v; \theta)$ and variance $\sigma^2(\mathbf{x}_v; \theta)$, with both terms predicted by our neural network. Directly modelling the aleatoric uncertainty in this way allows the model to control the relevance of noisy labels during training and thereby improve performance (Kendall and Gal, 2017). The output probabilities are computed by applying the Softmax function to samples drawn from this Gaussian:

$$\boldsymbol{\eta} | \mathbf{x} \sim \mathcal{N}(\boldsymbol{\eta}; \mu(\mathbf{x}; \theta), \sigma^2(\mathbf{x}; \theta)), \quad (6)$$

$$p(\mathbf{y}_v | \boldsymbol{\eta}) = \text{Softmax}(\boldsymbol{\eta})_v,$$

where $\sigma^2(\mathbf{x}; \theta)$ is a diagonal matrix. However, the log-likelihood no-longer has an analytical solution, so instead we use an Monte-Carlo approximation of the loss:

$$\mathcal{L}_{\text{HS}} = -\text{LSE}_{s=1}^S \left(\sum_{i=1}^V \sum_{c=1}^C \mathbf{y}_{ic} \log \text{Softmax}(\boldsymbol{\eta}_v)_c^{(s)} \right) + \log S, \quad (7)$$

where S is the number of Monte-Carlo samples, $\boldsymbol{\eta}^{(s)}$ is a sample from the logit distribution and LSE is the log-sum-exponent operator.

However, treating voxels as independent cannot yield spatially coherent samples. One simple approach that represents the spatially correlated nature of uncertainty

inherent to image segmentation (named Stochastic Segmentation Networks (SSN)) (Monteiro et al., 2020) models the joint distribution over voxels by replacing $\sigma^2(\mathbf{x}; \theta)$ with a covariance matrix $\Sigma(\mathbf{x}; \theta)$ over all pixels and classes. Due to the substantial size of a full covariance matrix, SSN utilises a low rank approximation $\Sigma(\mathbf{x}; \theta) = P(\mathbf{x}; \theta)P(\mathbf{x}; \theta)^T + D(\mathbf{x}; \theta)$, where $P(\mathbf{x}; \theta)$ is a $((V \times C) \times R)$ matrix, where R is the rank of $P(\mathbf{x}; \theta)$ and $D(\mathbf{x}; \theta)$ is a diagonal matrix.

2.2.6. Probabilistic U-Net

Probabilistic U-Net (Kohl et al., 2018) is an alternative approach to modelling the spatial aleatoric uncertainty in an image by with a conditional variational autoencoder (cVAE) extension of U-Net. It introduces a latent space \mathbf{z} , conditioned on the image, which is used to encode the potential variability in the segmentation. The distribution over segmentations is predicted by sampling \mathbf{z} from a learned prior network P with learned parameters ϕ : $P(\mathbf{z}|\mathbf{x}) = \mathcal{N}(\boldsymbol{\mu}_{\text{prior}}(\mathbf{x}; \phi), \boldsymbol{\sigma}_{\text{prior}}(\mathbf{x}; \phi))$. This latent variable is then combined with the output of the last U-Net layer in a small neural network f_{comb} with learned parameters γ which transforms \mathbf{z} into meaningful spatial variation and yields the final segmentation:

$$p(\mathbf{y}|\mathbf{x}, \mathcal{D}) = f_{\text{comb}}(f(\mathbf{x}; \theta), \mathbf{z}; \gamma). \quad (8)$$

However, the embedding space must encode useful spatial variations in the segmentation. To encourage this, during training a posterior network Q with learned parameters ω , conditioned on both \mathbf{x} and \mathbf{y} is employed, of the form $Q(\mathbf{z}|\mathbf{x}, \mathbf{y}) = \mathcal{N}(\boldsymbol{\mu}_{\text{posterior}}(\mathbf{x}, \mathbf{y}; \omega), \boldsymbol{\sigma}_{\text{posterior}}(\mathbf{x}, \mathbf{y}; \omega))$. To train the model the variational lower bound (ELBO) is minimized (equation (9)), which combines the cross entropy between the model predictions with \mathbf{z} generated from the posterior and the KL divergence between the prior and posterior distributions in a weighted sum with weight β :

$$\mathcal{L}_{\text{ELBO}} = \mathbb{E}_{\mathbf{z} \sim Q(\cdot|\mathbf{x}, \mathbf{y})} [-\log f_{\text{comb}}(f(\mathbf{x}; \theta), \mathbf{z}; \gamma)] + \beta D_{\text{KL}}(Q(\mathbf{z}|\mathbf{y}, \mathbf{x}) || P(\mathbf{z}|\mathbf{x})). \quad (9)$$

2.2.7. Stochastic Segmentation Networks Ensemble

Finally, we explore the complementary benefits of combining methods for modelling both epistemic and aleatoric uncertainty, which when combined may improve model performance Tanno et al. (2021). Due to their simplicity and efficacy, we combine SSN with deep ensembles. Specifically, we use an ensemble of SSN models. At inference time, we combine the elements of the ensemble uniformly:

$$p(\mathbf{y}|\mathbf{x}, \mathcal{D}) \approx \frac{1}{MS} \sum_{m=1}^M \sum_{s=1}^S p(\mathbf{y}|\boldsymbol{\eta}_m^{(s)}), \quad (10)$$

$$\boldsymbol{\eta}_m|\mathbf{x} \sim \mathcal{N}(\boldsymbol{\eta}; \boldsymbol{\mu}_m(\mathbf{x}; \boldsymbol{\theta}_m), \boldsymbol{\Sigma}_m(\mathbf{x}; \boldsymbol{\theta}_m)),$$

where $\boldsymbol{\eta}_m$ and $\boldsymbol{\theta}_m$ are the logits and parameters of ensemble element m respectively.

2.3. Calculating Uncertainty Maps

While some works do disentangle epistemic and aleatoric uncertainty, (Charpentier et al., 2022) (Laves et al., 2020), (Mukhoti et al., 2021a), attempting to disentangle uncertainty into separate components is difficult to achieve in a meaningful way (Wimmer et al., 2023) and here we simply assess the total (epistemic + aleatoric) uncertainty that each technique captures and the impact of the technique on model performance and generalisation. We utilise the predictive entropy to measure the total uncertainty (equation (11)). For stochastic techniques (i.e models that can produce multiple inferences for a given \mathbf{x}) we can view the technique as an injection of a noise vector \mathbf{z} (or uncertainty index) into a deterministic model, where different settings of \mathbf{z} introduce variations in the segmentations. For example, for an ensemble \mathbf{z} represents the choice of which element is used to produce the inference, while for SSN this is the sample from the distribution over logits (equation (6)).

$$\mathbb{H} \left[\mathbb{E}_{\mathbf{z} \sim p(\mathbf{z})} \left[p(\mathbf{y}_i|\mathbf{x}, \mathbf{z}) \right] \right] \approx \mathbb{H} \left[\frac{1}{S} \sum_{s=1}^S p(\mathbf{y}_i|\mathbf{x}, \mathbf{z}^{(s)}) \right]. \quad (11)$$

For Evidential DL, which is sample free, we calculate the predictive entropy of the predicted class probabilities (equation (5)).

2.4. Fazekas Estimation

Fazekas scores are widely used by clinicians to qualitatively and visually rate the WMH signal present in an MRI image (Cedres et al.) for cases where WMH are of suspected vascular origin. However, WMH volume and WMH segmentation features have been used to predict the Fazekas score Joo et al. (2022); mu et al. (2023). Fazekas scores range from 0 to 3 in two brain regions: periventricular (PV) and deep. It has been argued that WMH in both regions have different etiological and histopathological substrates, with WMH in the PV region exhibiting myelin loss and loosening of the white matter fibres, while in the deep these being more heterogeneous also involving ischaemic tissue damage reflected in multiple small cavities, and arteriosclerosis (Kim et al., 2008). They have also different correlates (Griffanti et al.). Evidence from analysing cardiovascular risk factors suggest WMH in the deep region are more strongly linked to ischemic damage while in the PV region they have been related to age-related neurodegenerative processes. Also, some argue they are simply different stages of vascular disease that begins in the PV region and progresses to the subcortical regions (Gronewold et al.). The high correlation between total WMH volumes and Fazekas scores Valdés Hernández et al. (2012); Joo et al. (2022) supports this argument. We refer to deep WMH as DWMH and periventricular WMH as PVWMH.

The four Fazekas categories for each region are described in (Fazekas et al., 1987). Briefly:

- 0: Absent or very minimal WMH.
- 1: WMH are discrete and diffuse. For DWMH punctiform, for PVWMH a very thin lining of WMH around the ventricles.
- 2: Substantial areas of WMH in both regions, exhibiting early stages of confluence, typically presenting as a halo surrounding the ventricles for PVWMH.
- 3: WMH are large and confluent, with extensive confluence across the DWMH. For PVWMH, large WMH are confluent with WMH in the deep area (making separation between DWMH and PVWMH unclear).

Figure 1 demonstrates the Fazekas categories where DWMH and PVWMH are identical. G.1 provides cases where DWMH and PVWMH Fazekas differ.

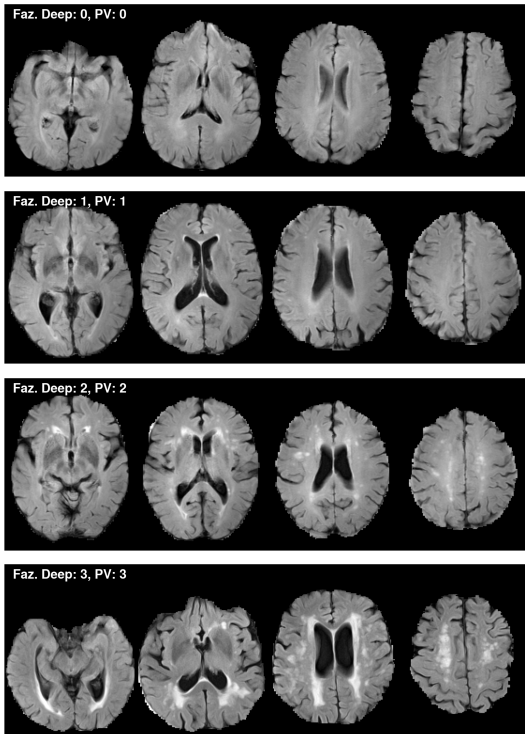


Figure (1) Fazekas Categories shown where Deep WMH = PV WMH. Examples taken from the ADNI dataset.

However, studies vary in their definitions on what to consider DWMH and PVWMH. Fazekas is perhaps best understood through a more general intuition, specifically that PVWMH refers to WMH that is contiguous with the ventricles, and that DWMH are simply separate or sufficiently distant from the ventricles (with some studies setting a threshold e.g 10mm), commonly referred to as the 'continuity rule' (Kim et al., 2008).

3. Materials and Methods

3.1. Data

We use T1-weighted and Fluid Attenuated Inversion Recovery (FLAIR) brain MRI data from four sources: 1) the

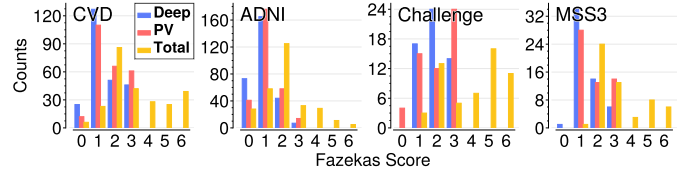


Figure (2) Distribution of Fazekas score per dataset, divided into the Deep, Periventricular (PV) and Total (combined) regions for each of the four datasets. Datasets appear in the following order: CVD, ADNI, Challenge and MSS3 from left to right

cerebrovascular disease (CVD) dataset, 2) the Alzheimer's disease neuroimaging initiative (ADNI), 3) the 2018 WMH segmentation MICCAI challenge and 4) the Mild Stroke Study 3 (MSS3). Figure 2 shows the distribution of the degree of WMH severity, given by Fazekas scores, for the four datasets. Images from the CVD dataset are used for training and testing, while those from the WMH segmentation challenge are used only for testing. The MSS3 and ADNI datasets are used for evaluating the robustness of UQ schemes to unseen data with different disease and population characteristics, and for assessing the usefulness of UQ schemes in the Fazekas classification task. MRI acquisition protocols for all data used in this work can be found in Appendix D.

3.1.1. CVD Dataset

The CVD dataset consists of data from 250 participants (88 females) in ageing and mild ischaemic stroke studies (Guerrero et al.) at the Centre for Clinical Brain Sciences at the University of Edinburgh. Mean (SD) age of the cohort is 71 (12), with the following distribution of vascular risk factors: 30 (12%) have diabetes, 174 (70%) are hypertensive, 139 (56%) have high cholesterol, and 145 (58%) are ex- or current smokers. In addition to WMH, 92 (37%) scans present one stroke lesion cluster and 66 (26%) present two. All images were acquired at a 1.5T GE Signa HDxt scanner, but by their acquisition protocols they can be grouped in 4 different unbalanced domains. The visual Fazekas scores (Fazekas et al., 1987) of WMH burden for the subset of this sample used for estimating Fazekas scores using UQ, are: median [QR1 QR3] equal to 1[1 2] for the deep white matter (Deep) region and 2[1 2] for the periventricular (PV) region.

3.1.2. ADNI Dataset

The Alzheimer's Disease Neuroimaging Initiative (ADNI) database (adni.loni.usc.edu) was launched in 2003 as a public-private partnership, led by Principal Investigator Michael W. Weiner, MD. The primary goal of ADNI has been to test whether serial magnetic resonance imaging (MRI), positron emission tomography (PET), other biological markers, and clinical and neuropsychological assessment can be combined to measure the progression of mild cognitive impairment (MCI) and early Alzheimer's disease (AD). We utilise a subset of this dataset, which

consists of structural brain MRI from 298 ADNI participants (136 females). Unlike the CVD and WMH segmentation challenge datasets, for which the data were deliberately selected from clinical studies to represent the breadth of WM disease found in individuals with sporadic SVD and the elderly, this dataset included data from all ADNI participants that in January 2016 had three consecutive MRI taken 12 months apart, with not just the T1-weighted MRI sequence, but also the rest of the structural sequences that allow for detection of SVD features. The data were extracted and screened for quality for previously published analyses (Valdés Hernández et al., 2018), (Harper et al., 2018). This subsample’s mean age (SD) is 72 (7.3) years old. Only 43 (14%) are hypertensive and 126 (42%) have endocrino-metabolic risk factors for Alzheimer’s disease (e.g diabetes, hypertension, hyperlipidemia, and obesity). In general, 249 (84%) had one or more cardiovascular risk factors. From the 59 ADNI imaging centers, 37 contributed with images to this subsample, which can be grouped in 13 unbalanced domains acquired from multiple MRI scanner models. This dataset is unseen during training of the WMH segmentation and UQ techniques, and is utilised for the Fazekas classification task and qualitative analysis. Fazekas scores (in the subset used for Fazekas prediction) given as median [QR1 QR3] for the Deep region are 1[0 1], and 1[1 1] for the PV region.

3.1.3. WMH Challenge Dataset

This dataset belongs to the publicly available MICCAI WMH Segmentation Challenge (Kuijf et al.). It consists of T1-weighted, FLAIR, and WMH ground-truth images from 60 patients, 20 of who were imaged from 3 separate sites with different acquisition parameters. For this work, the Fazekas scores were for the Deep region 2[1 2.5] and 2[1 3] for the PV region.

3.1.4. MSS3 Dataset

MSS3 (Clancy et al.) is a prospective observational cohort study to identify risk factors for and clinical implications of SVD progression. We use a subsample of 65 patients (16 females) aged 67.6 (19.7) years, with Fazekas PV scores of 1[1 2.5] and deep region scores of 1[1 2]. Explanation of the segmentation pipeline can be found at (Valdés Hernández et al., 2023).

3.2. Data Preprocessing

Brain extraction was performed using ROBEX Iglesias et al. (2011) to all datasets except CVD where the intracranial volume binary masks provided were used. Correction from b1 magnetic field inhomogeneities was performed to the T1-weighted images from all datasets using FSL-FAST (Zhang et al., 2001). Given the multi-domain nature of all datasets used, we resampled all images to 1 x 1 x 3 mm³ voxel size (i.e., the median voxel size of the sample) using 3rd-order B-spline interpolation. WMH ground-truth masks from the CVD and WMH segmentation Challenge datasets were resampled using nearest

neighbour interpolation. We aligned both MRI sequences in the ADNI dataset using Simple-ITK (Lowekamp et al., 2013) (all other images were spatially aligned when these datasets were accessed). Z-score intensity normalization (Reinhold et al., 2019) was applied to each scan sequence per patient.

Supplementary C.1 shows the voxel intensities for the CVD, ADNI and Challenge datasets pre and post z-score normalization. After normalization, we see that the histograms of the FLAIR intensities in each dataset and subdomain can be approximated as a bimodal distribution, with a large peak centered slightly right of 0 and a lower peak below zero. The relation between the histograms’ peak of each mode differs between the datasets, with the WMH Challenge dataset showing the clearest distinction between the two modes, while the CVD and ADNI datasets peak mainly around the positive mode (i.e closer to a unimodal negative skewed distribution). Along with the variations in cohort selection and Fazekas distributions these datasets represent real world differences in input distribution through which we shall assess the generalisation performance and utility of the examined UQ techniques.

3.3. Backbone Segmentation Method

We assess each UQ technique using a U-Net segmentation architecture with residual connections in each block adapted from (Mojiri Forooshani et al.). The U-Net architecture is an effective and parameter efficient architecture in many segmentation tasks (Isensee et al., 2021). We use the same backbone architecture for all our tests. To increase the effective sample size of the training data, we use augmentation procedures similar to previous work on the WMH challenge dataset (Park et al., 2021), including random flipping in the sagittal plane (p=0.5), affine transformations (each p=0.2) such as rotation (-15°, 15°), shearing (-18°, 18°), translation with ratio (-0.1, 0.1). We utilise a 70/15/15 % train, validate test split on the CVD dataset. Splits are performed on 3D images, after which we use 2D axial slices for training the model. All evaluation is performed in 3D. After performing an initial hyperparameter search (see section 3.4) on the validation set, we then apply 6-fold cross validation, utilising the same split proportions. All 6 cv-fold runs are evaluated on the Challenge dataset to assess OOD segmentation performance. For the UQ methods that express uncertainty via producing different inferences (samples) for the same input, to generate 3D samples, we order the samples over each 2D slice by volume, such that sample n contains the n th largest sample of each slice. This promotes diversity of sample volume and allows us to estimate the range of WMH volumes over the whole brain implied by the model. We provide our code here².

²<https://github.com/BenjaminPhi5/wmhuq>

3.4. UQ Method Specific Implementation

We begin with training a baseline deterministic segmentation model, trained with the combo loss (Taghanaki et al., 2019), which is a sum of the cross entropy and soft Dice score loss (we use an equal weighting). We reuse combo loss or an equivalent for consistent comparison between methods. The choice of loss function can effect not just the calibration of a given model but the utility of the resulting uncertainty map (Philps et al., 2023). Since many axial slices contain no WMH, we tuned the proportion of empty slices that are retained in the training data, selecting from the set 0.05, 0.1, 0.3, 0.5, 0.9, 1. We found that a retention proportion of 0.1 was optimal. For each UQ technique, we separately tuned the learning rate in the set 0.01, 0.001, 0.0001 and weighted decay in between $[0, 1e - 2]$ to prevent overfitting. We multiplied the learning rate by 0.5 every 50 epochs until the learning rate reaches $2e - 5$. Training stops if there has been no improvement in the validation loss for 100 epochs. We use a batch size of 32 for all experiments. Below we outline extra hyperparameter tuning applied to each method on the validation data, after selecting the parameters that yielded the strongest performance on the majority of the following metrics [Dice, Best (Highest) inference Dice, AVD, Best (lowest) inference AVD] unless otherwise specified.

3.4.1. MC-Dropout (MC-Drop)

We tuned the dropout rate, from [0.05, 0.1, 0.2, 0.3 0.4] applied to {encoder only, all, or decoder only} layers. We found that using all with a rate of 0.2, yields the highest sample diversity and the strongest Dice performance. Applying dropout to only part of the network architecture significantly reduced the sample diversity and could lead to poor performance on metrics such as D_{GED}^2 (see 3.5.2). Due to the regularizing effect of Dropout, weight decay was not necessary.

3.4.2. Deep Ensembles (Ens)

We initially adjusted the number of elements in the ensemble in the range [3, 5, 10, 20, 30], finding that 10 presents a suitable balance between performance and training time. Using a smaller ensemble significantly reduced the sample diversity expressed by the ensemble, with diminishing returns in increasing the ensemble size beyond 10.

3.4.3. Evidential Deep Learning (Evid)

To retain the combo loss for the evidential DL UQ scheme, use the sum of equations (3), (2), (4). We further tune a weighting parameter for the KL component (equation (4)) from the set 0, 0.01, 0.05, 0.1, 0.5, 1 finding 0.05 yields the strongest performance. We initially adjusted the value of the KL term in the loss on a logarithmic scale between 0 and 10. For stability during training, we increase the KL term from 0 to its target value over the first 50 epochs.

3.4.4. Stochastic Segmentation Networks (SSN)

We initially adjusted the rank of the covariance matrix, trying values of [5, 10, 12, 15, 18, 20, 25, 30, 40, 50] with 25 yielding strong performance. Lower ranks reduced the expressiveness of the sample distribution (i.e highest Dice amongst multiple inferences) while higher ranks produced marginal to non-existent gains. We also train a model with rank of 1 (diagonal covariance) for the variant where voxels are treated as independent (equation (6)) - we refer to this variant as (Ind).

3.4.5. Probabilistic UNet (P-Unet)

We initially adjusted the KL term between 0 and 10 on a logarithmic scale, finding 1 most effective. We tune the size of the latent dimension \mathbf{z} (see Section 2.2.6) in 6, 12, 24, 36 finding 12 to as effective as 24 or 36. To compute the combo loss, we add the soft Dice component to the ELBO (equation (9)) using \mathbf{z} generated from the posterior network. We employed the existing implementation of P-Unet(Kohl et al., 2018), and modified it to integrate it with our segmentation backbone.

3.5. Evaluation Metrics

To assess the generalisation of our methods, we present all our comparisons on unseen datasets as well as the standard hold-out test fold of the training distribution.

3.5.1. Top Sample

To assess the segmentation quality of each technique, we apply the Dice score and the Absolute Volume Difference (AVD) to assess spatial and volumetric alignment with the ground truth. For the techniques that generate multiple inferences (samples) per input \mathbf{x} , we also report the highest scoring inference for Dice and AVD. A method that produces a meaningful distribution of WMH segmentations should ideally contain a sample very close to the ground truth within a small number of samples. This for example may allow a user to select an output from a range of possible segmentations.

3.5.2. Generalised Energy Distance

Assessing pixelwise calibration fails to capture structural variance expressed by a segmentation model (i.e differences in boundary shape). We compute the generalised energy distance (Székely and Rizzo, 2013), which measures the distance between the predicted distribution and the ground truth distribution and a commonly used metric for assessing sample quality (Czolbe et al., 2021), (Monteiro et al., 2020): $D_{\text{GED}}^2(p, \hat{p}) = 2\mathbb{E}_{y \sim p, \hat{y} \sim \hat{p}}[d(y, \hat{y})] - \mathbb{E}_{y, y' \sim p}[d(y, y')] - \mathbb{E}_{\hat{y}, \hat{y}' \sim \hat{p}}[d(\hat{y}, \hat{y}')]$, where d is a distance metric, e.g $d(a, b) = 1 - \text{IOU}(a, b)$.

3.5.3. sUEO Score

Uncertainty maps should precisely identify regions with errors. The uncertainty error overlap (UEO) metric assesses overlap between uncertainty and segmentation error by computing the Dice metric between a thresholded

uncertainty map and the error in the mean segmentation (Jungo et al., 2020). This rewards uncertainty that is well localised to the segmentation error. Soft Uncertainty-Error Overlap (sUEO) (Li et al., 2022), uses a soft Dice score to provide a threshold free evaluation of overlap between uncertainty and overlap. sUEO is defined as:

$$\text{sUEO} = \frac{2 \sum_i e_i u_i}{\sum_i e_i^2 + u_i^2}, \quad (12)$$

where e_i is the segmentation error at pixel i : $e_i = \text{argmax}_c p_{ic} \neq y_i$. Higher sUEO denotes greater overlap.

3.5.4. Patchwise Uncertainty quality metrics

The sUEO metric assess the uncertainty at an image level. To assess the uncertainty map at subregions within the image, we use the patchwise uncertainty quality metrics proposed in prior work (Mukhoti and Gal). Ideally, our model should be accurate when it is certain and by extension uncertain when it is inaccurate. The probability that a model is accurate when it is certain, $p(\text{acc}|\text{cert})$, and the probability that a model is uncertain when it is inaccurate, $p(\text{uncert}|\text{inacc})$, are calculated by counting regions in the image where the model is accurate or inaccurate, and certain or uncertain respectively. To do this, we divide the image into patches of size 4^3 . For each patch, it is accurate if the proportion of accurately segmented voxels is ≥ 0.8 . We plot how these metrics change as we change the uncertainty threshold τ (patches are uncertain if the average uncertainty in the patch is $\geq \tau$). Finally, the PAvPU (Patch Accuracy vs. Patch Uncertainty) metric (Mukhoti and Gal) combines these two metrics:

$$\text{PAvPU} = \frac{n_{ac} + n_{ui}}{n_{ac} + n_{ui} + n_{au} + n_{ci}}, \quad (13)$$

where n_{ac} refers to the number of patches that are accurate and certain, n_{ui} for patches that are uncertain and inaccurate, n_{au} for patches that are accurate and uncertain, and n_{ci} for patches that are certain and inaccurate.

3.5.5. Missing Lesion Coverage

WMH can be very small, particularly for cases with thin pencil-like periventricular lesions and deep isolated WMH. However aleatoric uncertainty is high for such lesions due to their relatively high proportion of edge voxels to total voxels and their subjective nature. Furthermore, small lesions can be easily missed by the model, which can result in silent failure, where the lesion is missed in the segmentation, and not highlighted as uncertain either. To assess the coverage of false negatives in the uncertainty map and lesion-wise silent failure rates, we calculate three metrics. First, we calculate the false negative coverage (per voxel) in the uncertainty map. Second, we calculate the proportion of instances that are undetected (missed) in both the mean predicted segmentation and the uncertainty map. We define instances as 3D connected components in a binarized image, and an undetected instance as an instance

where no voxels in the segmentation or thresholded uncertainty map overlap with the instance. Similarly, we define detected instances where at least one voxel in the predicted segmentation or thresholded uncertainty map does overlap with the instance. Finally, we compute the size of missed instances.

3.6. Downstream task 1: Predicting Fazekas

In this subsection we outline our methodology for utilising WMH segmentation maps and uncertainty maps to predict the clinically useful Fazekas score, across multiple datasets with different cohort and disease characteristics. To do this, we will utilise the outputs from our models pre-trained on the CVD dataset to perform WMH segmentation, after which we extract a series of features (outlined below) from the outputs. Due to the lack of WMH reference segmentations available for the ADNI dataset, we cannot directly assess the generalisability and robustness of our WMH segmentation models on this dataset. However, we use the ADNI dataset for Fazekas prediction as a way to validate our method on a data distribution which is unseen during training the WMH segmentation models.

In order to predict Fazekas, we shall use our extracted features to fit a logistic regression model, for the CVD and ADNI datasets. In order to assess whether the choice of segmentation model impacts classification performance, we shall extract features from a baseline deterministic model, as well as UQ techniques. The subsections below detail the rationale behind the feature extraction process and statistical methodology undertaken.

3.6.1. Feature Extraction Rationale and Thresholding

Due to the relatively small size and high class imbalance of each dataset we extract distributional and spatial features from our model outputs to train a logistic regression model to predict Fazekas. Below we outline each of the features extracted and their rationale.

Given that WMH volume is a known predictor of both DWMH and PVWMH Fazekas score (Andere et al.), we calculate the sum of voxel intensities in the thresholded maps. However, as Fazekas is also defined by the spatial position and confluence of WMH, we devise a feature extraction technique to capture all these components. First, we generate rings around the ventricles, at a distance of $< 5\text{mm}$, between 5mm and $< 10\text{mm}$, between 10mm and $< 15\text{mm}$ and finally $\geq 15\text{mm}$ away from the ventricles (Figure 3). SynthSeg (Billot et al., 2023) is used for ventricle segmentation. For each region, we extract the total volume, the number of connected components per volume, and the standard deviation of connected components per volume. We further extract the largest connected component that includes both the 1st and 2nd ring as well as the 2nd and 3rd ring, in order to assess confluence. To assess the utility of the uncertainty information in improving the Fazekas score, we also extract the same features from the uncertainty map of each method. We further extract

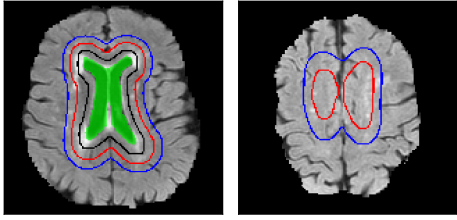


Figure (3) Ventricle rings used in the feature extraction stage for the Fazekas / QC prediction tasks. Green shows the ventricle segmentation. Black, Red and Blue lines show euclidean distances of 5, 10 and 15 mm from the ventricles respectively. Example taken from the Challenge dataset.

the standard deviation of each feature across 10 inferences generated from sample-based UQ methods.

3.6.2. Model Training and Hyperparameter Tuning

There are two key hyperparameters in our method for predicting Fazekas scores. The first is the threshold at which we filter out information from the segmentation and uncertainty maps, prior to calculating the features from the previous section. For a given threshold t we set all voxels with an intensity below t to 0. The second is the total number of possible features we could provide to the model, which is large. To prevent overfitting, we employ recursive feature elimination, where we train a model on the feature set multiple times, each time removing the least important features (by assessing their weight in the model) until we have k features remaining. To avoid a biased selection of the hyperparameters, we run the experiment for settings of t in 0.1, 0.2, 0.3 and k for all integers between 10 and 20, and report the results across all possible hyperparameter settings.

All features are z-score normalized, with the mean and standard deviation calculated excluding values above the 95th percentile to reduce the impact of outliers. Values above the 95th percentile are clipped to the 95th percentile prior to normalization. We use a multivariable logistic regression model for predicting Fazekas score, with a balanced cross-entropy loss that reweights the loss of each class (i.e., score) inversely proportional to the number of elements of that class. While reweighting the loss may reduce the overall accuracy of the model across the entire cohort, achieving greater separation between Fazekas scores of 0,1 and of 1,2 (Fazekas 1 is the dominant class) is arguably more useful. This allows us to better detect patients who have less visible white matter disease (Fazekas 0) and patients who already demonstrate more severe WMH (Fazekas 2 and 3), which has been associated with cognitive dysfunction, and it is useful for identifying patients with increased risk of cerebrovascular disease (Cedres et al.; Wardlaw et al.). We use a regularization strength (weight decay) of 10 to prevent model overfitting.

To assess the generalisability of our models, we conduct two experiments. For the first, we build a train and test dataset by combining the CVD, ADNI and Challenge datasets, with a 85%/15% train test split. For the second

experiment, we swap the Challenge and MSS3 dataset, so that the Challenge is now an unseen OOD dataset. We leave the MSS3 dataset as an OOD test dataset. When using the CVD dataset, we only extract predictions and UQ maps from models for which the given image was in the test fold during the original model training. For all other datasets, we used the models trained from the first cross validation fold).

3.7. Downstream task 2: Quality Control

We wish to explore the usefulness of different methods for identifying poor quality segmentations, hereon referred to as the QC task. We setup a binary classification task. We define images with Dice ≤ 0.57 as ‘poor quality’ (this corresponds to images in the bottom 20th percentile in the CVD test set) and all other images are ‘good quality’. We use the same feature extraction and model training process as for the Fazekas classification task. The model is trained on the CVD dataset and evaluated with the Challenge dataset, using the performance of the SEnt model to derive the class labels. Due to the smaller number of images available during training than those available for the Fazekas scoring task, we restrict k in the range [6, 12].

4. Results

4.1. UQ techniques improve model robustness and reduce silent failure rates in UQ maps

First we inspect the segmentation performance of each method. As we are interested in the generalisation performance of our methods, we primarily assess performance on the OOD (Challenge) dataset, with equivalent results for the held out in-distribution test found in Appendix A. Table 1a shows the segmentation performance metrics. All methods outperform the baseline SEnt Dice score, however the methods that do not model epistemic uncertainty do not yield an improved AVD% score over the baseline, despite yielding stronger performance in the in-distribution held-out dataset (A.1a). Nonetheless, modelling both uncertainty components provides complementary performance benefits, with SSN-Ens yielding higher precision over recall (Figure 4) and Dice (0.70) over modelling just aleatoric (SSN - Dice 0.68) and epistemic (Ens - Dice 0.69) vs baseline SEnt Dice of 0.67 as well as yielding the highest Top Dice (0.72) and lowest Top AVD% (12.3). MC-Dropout also yields meaningful variation between model inferences, improving AVD% from 46.5% for the mean prediction to 23.9% for the best sample, suggesting that Dropout layers early in the model contribute to substantial structural changes in the segmentation. Unsurprisingly, Ind is unable to express meaningful differences in the quality of segmentation with minimal differences in the Top vs mean Dice and AVD% in both datasets. The sample diversity of P-Unet is also poor, with limited improvement in Top AVD% over AVD%. The SSN-Ens model is more consistent across model runs, with smaller

confidence intervals 1a and yields less low Dice outliers than other methods in both in-distribution and OOD data (see B.1a and B.1b).

Table 1b demonstrates the uncertainty quality scores. P-Unet yields the strongest sUEO (0.5) score while methods that perform the strongest on the Top AVD% metric (i.e Ens, SSN, SSN-Ens) yield lower sUEO score (0.46) than the baseline 0.47. We see this is opposite to the D_{GED}^2 where SSN-Ens yields the best (lowest) score (0.63) while P-Unet (0.87) and Ind (0.89) perform very poorly, as methods with high sample diversity achieve lower D_{GED}^2 (Figure 9).

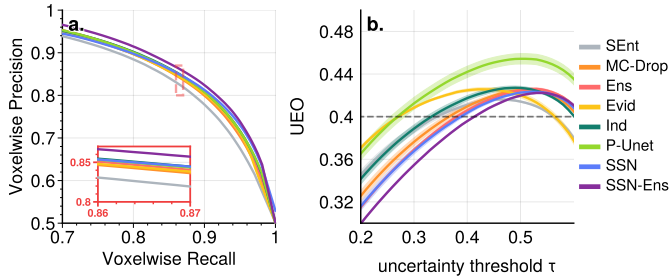


Figure (4) Voxelwise precision vs recall for WMH classification in the OOD (Challenge) dataset. Red box shows zoomed in view of the dashed region to demonstrate the ranking of method performance. (b) Mean Uncertainty error overlap (UEO) as τ changes for the OOD (Challenge) dataset. Dotted line shows UEO at 0.4.

While sUEO rewards strong localisation of errors, this does not differentiate between uncertainty around the boundaries of large WMH and the coverage of deep isolated WMH, which are proportionally insignificant but important indicators of lesion growth. sUEO hence inherently favours models that introduce less uncertainty around correctly identified voxels at the cost of detecting small WMH. Figure 5 (top) shows the patchwise uncertainty quality and lesion coverage metrics. SSN-Ens yields the highest score for $p(acc|cert)$ and $p(uncert|inacc)$ across all thresholds, while P-Unet performs the strongest and SSN-Ens the weakest on the PAVPU metric (due to the high number of uncertain but accurate voxels and hence low UEO score at low τ (Figure 4)). When adjusted for equivalent UEO scores, SSN-Ens yields now the poorest performance on $p(acc|cert)$ and $p(uncert|inacc)$ metrics (while the strongest performance on the combined PAVPU metric), due to the high threshold needed to reduce the number of uncertain accurate voxels.

Figure 5 (bottom) shows the results for the detection of unsegmented WMH lesions. While SSN-Ens yields consistently the highest coverage of unsegmented WMH regardless of τ (a), when adjusted for UEO it is comparable to P-Unet. SEnt is the worst performer with the lowest coverage proportion, and highest proportion and size of undetected lesions, with the gap between the UQ techniques and SEnt increasing once adjusted for equivalent UEO scores. Hence, the patch-wise metrics (where SEnt has midpack performance) are not suitable for assessing instance-wise coverage. In (b) we see that as we

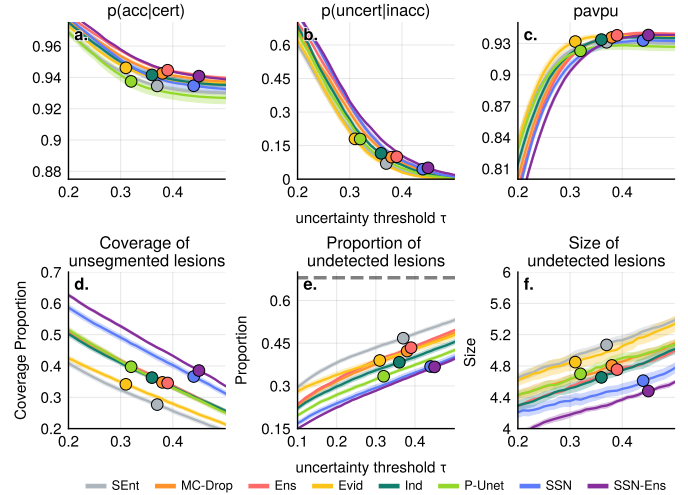


Figure (5) (a-c) Patchwise uncertainty metrics as τ changes for the OOD (Challenge) dataset. All metrics computed with a sliding window size of 4^3 voxels and accuracy threshold of 0.8. (a) Probability that a patch is accurate given that it is certain. (b) Probability that a patch is uncertain given that it is inaccurate. (c) PAVPU metric. (d-f) Lesion Instance Coverage metrics for the OOD (Challenge) dataset. Instances are 3D connected components in the ground truth WMH mask. (d) Coverage of unsegmented lesions: The mean proportion of unsegmented instances which are deemed uncertain. (e) Proportion of undetected lesions: The proportion of instances for which less than 50% of the instance (or less than 5 voxels, whichever is lower) are deemed uncertain and are segmented. Dashed line shows the number of instances which are undetected for baseline model SEnt in the WMH segmentation. Most instances are < 10 voxels in volume and undetected. (f) The size of undetected instances. For all plots, the shaded area denotes the standard error over the 6 model runs, and the circles indicate the point at which each method attains an Uncertainty Error Overlap (UEO) of 0.4 on the CVD dataset.

increase τ the proportion of lesions that are entirely undetected (a ‘silent failure’ of the UQ map) increases sharply, as detecting the smallest lesions comes at the cost of introducing a large number of TP and TN voxels as uncertain. The mean size of entirely undetected lesions is lowest among the methods that utilise Gaussian distributions over the logit space to model aleatoric uncertainty (Ind, SSN, SSN-Ens). Nonetheless all methods silently fail for between 30% to 50% of lesions at an equivalent UEO threshold (UEO = 0.4 in CVD dataset) in both in-distribution (CVD) and OOD (Challenge) data.

We have examined results across the different cohorts, however UQ performance varies greatly between individuals within the same cohort. Crucially, SSN-Ens attains the best Top AVD% score due to consistent performance across all volumes, while the performance of P-Unet degrades as WMH volume decreases (Figure 6). The low sample diversity expressed in low volume subjects by P-Unet produces fewer uncertain but accurate voxels, yielding higher sUEO for low WMH volume subjects (c), while also explaining the high performance on the PAVPU metric and higher UEO at a given τ (Figure 6). Finally, we find that across almost all metrics evaluated in this section the order of model performance seen in the Challenge data

Table (1) (a) Mean Segmentation performance of each technique on the OOD (Challenge) dataset. Sample Dice/AVD refer to the best score attained from the 10 samples (forward inferences) generated from each model. (b) Uncertainty quality metrics for the OOD (Challenge) dataset. sUEO: Soft Uncertainty Error Overlap. D_{GED}^2 : Generalised energy distance. 95% confidence interval is calculated over the 6 model runs. Best results are shown in bold.

(a) Segmentation performance					(b) Uncertainty map performance		
	Dice	Top Dice	AVD%	Top AVD%		sUEO	D_{GED}^2
SEnt	0.67 ± 0.01	—	50.2 ± 6.7	—	SEnt	0.47 ± 0.00	—
MC-Drop	0.68 ± 0.00	0.70 ± 0.00	46.5 ± 4.8	23.9 ± 4.2	MC-Drop	0.47 ± 0.01	0.73 ± 0.01
Ens	0.69 ± 0.00	0.69 ± 0.00	42.7 ± 1.7	19.2 ± 2.7	Ens	0.46 ± 0.00	0.66 ± 0.01
Evid	0.68 ± 0.01	—	49.2 ± 8.0	—	Evid	0.48 ± 0.00	—
Ind	0.69 ± 0.01	0.69 ± 0.01	50.1 ± 7.9	48.1 ± 7.8	Ind	0.48 ± 0.01	0.89 ± 0.02
P-Unet	0.68 ± 0.01	0.69 ± 0.01	55.4 ± 13.0	39.2 ± 8.8	P-Unet	0.50 ± 0.01	0.87 ± 0.02
SSN	0.68 ± 0.01	0.71 ± 0.01	55.0 ± 11.5	17.3 ± 5.5	SSN	0.46 ± 0.00	0.71 ± 0.03
SSN-Ens	0.70 ± 0.00	0.72 ± 0.00	43.8 ± 3.1	12.3 ± 1.5	SSN-Ens	0.46 ± 0.00	0.63 ± 0.01

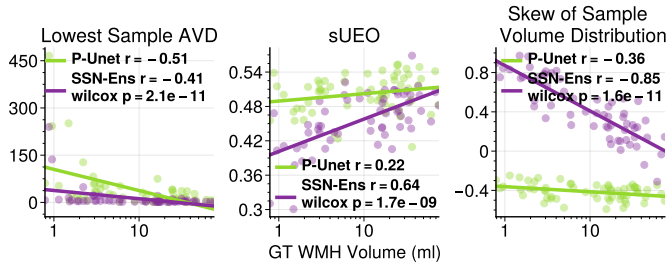


Figure (6) Comparison of P-Unet and SSN for each subject in the OOD (Challenge) dataset, reporting Pearson correlation coefficient and Wilcox signed-rank test. Lowest Sample AVD score: SSN-Ens exhibits consistently lower (better) top sample AVD score ($p = 2.1e-11$) sUEO score: P-Unet exhibits consistently higher (better) soft Uncertainty Error Overlap (sUEO) score than SSN-Ens ($p = 1.7e-9$).

matches the in-distribution test data (Appendix A).

4.2. UQ techniques robustly improve the prediction of the Fazekas score

In this section we examine the predictive power of spatial and uncertainty features extracted from the WMH segmentation and UQ outputs of our models in the Fazekas prediction task. Figure 7 shows the results of different feature selection criteria across all hyper-parameter settings of the classification model for the (a) DWMH and (b) PVWMH model for both in distribution test and OOD test data. Results across both choices of OOD dataset (MSS3/Challenge) are combined, however separate results can be found in Figures H.1 (MSS3) and H.2 (Challenge). We compare Accuracy and Balanced Accuracy (class weighted) and macro-averaged F1 score to assess classification performance, and multi-class root mean brier score to assess model calibration. Within in-distribution test data, using only predicted WMH volume is the worst predictor for both Deep and PV categories with a median (across all hyperparameter settings) balanced accuracy of 0.60 and 0.73 respectively. The addition of spatial features from the SEnt model always improving performance, with median balanced accuracy of 0.66 and 0.77 in the Deep and PV regions respectively. Crucially, adding UQ specific features from either P-Unet or SSN-Ens always yields a significant improvement across all metrics over features from the SEnt model (with median balanced accuracy of

0.71 and 0.82 in the Deep and PV regions respectively for the SSN-Ens variant), and from the equivalent UQ method with only WMH segmentation features (except for Balanced Accuracy for SSN-Ens vs SSN-Ens w/ UQ for DWMH). Using UQ features from SSN-Ens yields significant improvements across all metrics over P-Unet UQ features for the DWMH task in both in-distribution and OOD data. For PVWMH on in-distribution data there is no significant difference between SSN-Ens and P-Unet UQ features. This may be explained by the difference in sample diversity and small WMH coverage in the UQ map between methods; while WMH in the PV region follow a common pattern of shape and location, small WMH in the Deep region are highly spatially varied, with the vast majority of small WMH in the Deep region and hence identification of possible WMH locations in DWMH implying a greater range of plausible DWMH volumes. This may be important when the implicit threshold between NAWM and WMH varies between annotators conducting a Fazekas annotation from MRI images.

For both PVWM and DWMH, performance drops notably in the OOD across both tasks, with the volume-only model outperforming the SEnt model for PVWMH across all metrics. While ordering of feature-set performance is broadly preserved for the DWMH task, for PVWMH there is no obvious top feature-set candidate. However we observe that this is most likely caused by differences in the considerations followed by annotators across different datasets while generating the Fazekas scores. Figure I.1 demonstrates in-distribution vs OOD confusion matrices for the SSN-Ens w/ UQ feature set and Figure I.2 shows the WMH volume as a proportion of brain volume for each Fazekas category. In the MSS3 dataset, the median WMH proportion for DWMH 0 class subjects is approximately equal to that of the DWMH 1 median WMH proportion. Consequently, when assessing a model on the MSS3 dataset for DWMH prediction that hasn't seen MSS3 during training, most DWMH 1 images will be classed as Fazekas 0. For PVWMH, the difference in WMH proportion per class c is so severe that each class in MSS3 is approximately equivalent to the distribution of class $c-1$ in the CVD dataset, with no class 0 present in the dataset. Hence, the model predicts a Fazekas score 1 lower than the

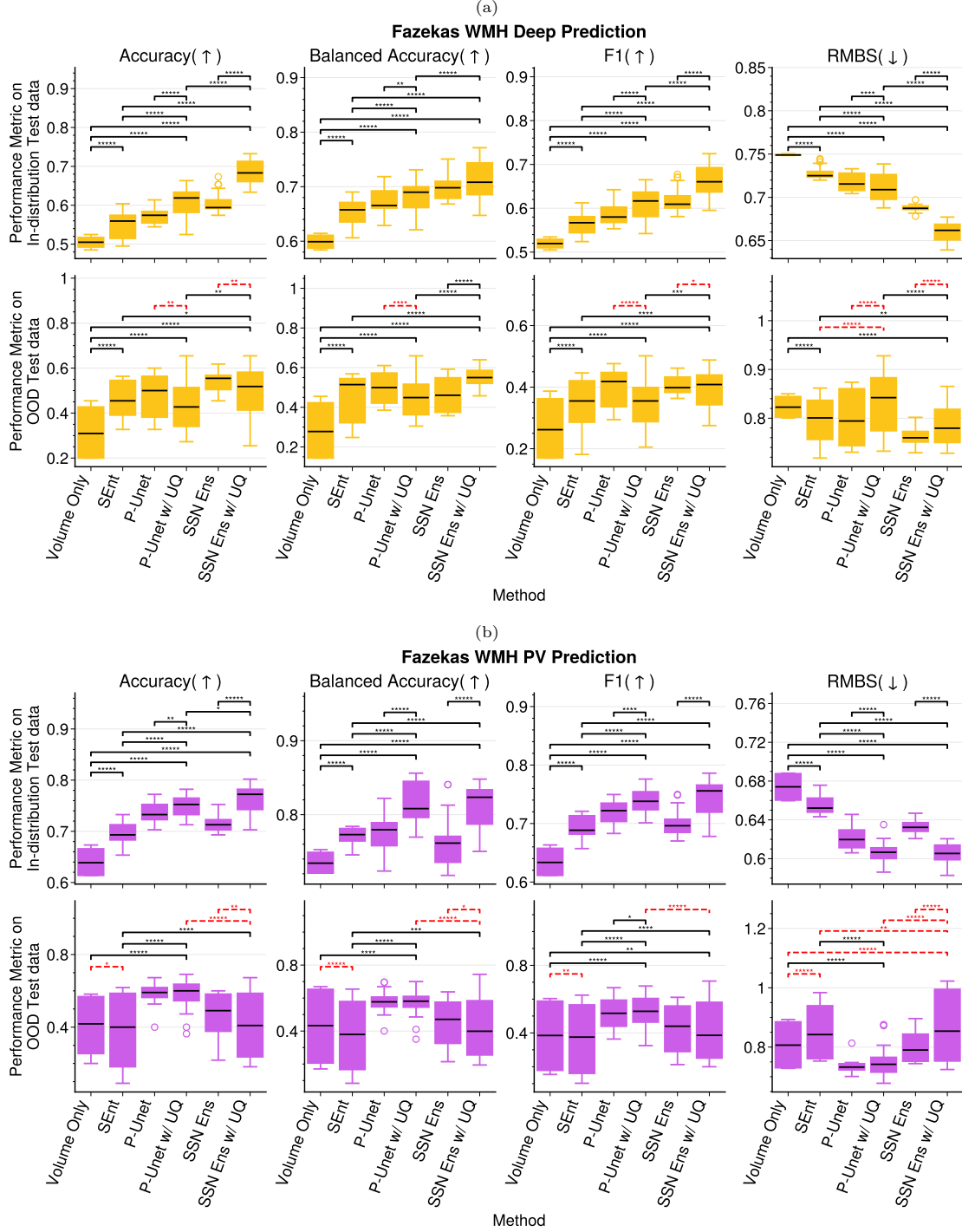


Figure (7) Distribution of Fazekas prediction scores for (a) the WMH Deep and (b) the PVWMH prediction task. For each technique, the plotted distribution shows the range of scores across all hyperparameter settings. F1: macro-averaged F1 score. RMBS: multi-class root mean brier score. The four methods are: Volume Only: prediction model using only the predicted WMH volume from the SEnt model. SEnt: Using spatial and regional volumetric features extracted from the WMH prediction from the SEnt model. SSN-Ens w/UQ: Using features extracted from both the WMH prediction, UQ map and distribution of features over multiple inferences for the SSN-Ens model. P-Unet w/UQ: Using features extracted from both the WMH prediction, UQ map and distribution of features over multiple inferences for the P-Unet model. Pairwise two-tailed t-test between each set of methods (comparing equivalent hyper-parameter choices between each method) **excluding** P-Unet and SSN Ens which are compared only to their variants with UQ features. Significance shown with ($p < 0.05$: *), ($p < 0.01$: **), ($p < 0.001$: ***), ($p < 0.0001$: ****), ($p < 0.00001$: *****). Black line/* denotes the right hand model shows significant improvement over left hand model; dotted red line/* denotes left hand model shows significant improvement over right hand model. If no line is shown no significant pairwise relationship between methods is found.

ground truth in the majority of cases. Finally, while there is closer alignment in WMH proportions between the Challenge and CVD datasets, the median WMH proportion of PVWMH Fazekas 3 in the Challenge dataset is almost half that ($\simeq 0.02$) of the WMH proportion in the CVD dataset ($\simeq 0.04$) and consequently there is considerable confusion between the PVWMH 2 and 3 classes when attempting to generalise a model to the Challenge dataset.

4.3. UQ techniques improve Quality Control and Volume Estimation of WMH segmentation

We now examine the QC classification task. Figure 8 demonstrates the (a) accuracy and (b) F1 score for each feature set. In (c) we perform a filtering of the test data where images with a probability of being poor quality is $< p$ are removed from the dataset, and evaluate how the number of filtered vs remaining poor quality images in the dataset changes as p increases. Similarly to the Fazekas score, using volume information is consistently the least informative feature set for detecting poor quality segmentations. Crucially, using UQ features from the SSN-Ens model yields significant improvements in accuracy and F1 score over using only WMH segmentations from either the SSN-Ens model or the SEnt model, or the volume based classifier. In the filtering task, there is a clear distinction between the SSN-Ens with UQ features compared to all other settings, while features from P-Unet yield an almost identical filtering curve to the spatial features from the SEnt model. Figure 9 explores how the distribution of WMH volumes predicted by the stochastic method varies as the ground truth WMH volume changes. At low WMH volumes all methods consistently overestimate the WMH burden in the median segmentation. However, methods with low D_{GED}^2 exhibit high sample diversity, such that the distribution of volumes predicted by the model is more likely to include the ground truth. P-Unet exhibits minimal sample diversity at individuals with low WMH volume, while Ind exhibits almost none across the whole range of volumes, as expected. Mc-Dropout shows a broader range, but like P-Unet and Ind, if the median is far from zero, the range of possible volumes predicted cannot match the ground truth. Furthermore, the skewness of the distribution of WMH volumes from SSN-Ens increases as volumes are smaller (Figure 6). Hence we can correct for poor model performance at low volumes automatically by selecting a low volume segmentation from the predicted WMH distribution. This explains why the UQ representation from SSN-Ens can be used to effectively detect poor quality segmentation, while P-Unet UQ features with low sample diversity do not yield equivalent gains.

4.4. SSN-Ens provides semantically meaningful UQ maps that identify stroke lesions and segmentation errors

So far we have shown that UQ techniques improve the robustness and generalisation of WMH segmentation models, Fazekas classification and identification of poor quality images. We now examine the semantic information

captured by the UQ maps of the top performing method (SSN-Ens) vs the baseline SEnt in the MSS3, Challenge and ADNI datasets.

We first examine images with known stroke lesions in the MSS3 dataset (Figure 10a and Appendix E). SSN-Ens is able to highlight areas where there is a stroke lesion within the spatial distribution of WMH as uncertain. Crucially, SSN-Ens highlights stroke lesions (that lie within the spatial and shape distribution of WMH) as uncertain. However SEnt is likely to segment stroke lesions as WMH and often erroneously identifies only the boundary of the lesion as uncertain. SEnt may even erroneously highlight the cavitated region of stroke lesions as uncertain (E.2b), when these are clearly not WMH, leaving the rest of the lesion certain. While this suggests uncertainty quantification may be able to improve discerning between WMH and stroke lesions, stroke lesions outside the spatial and shape distribution of WMH are, as expected, not segmented and not uncertain (E.2a, E.3b), and hence require training models with additional stroke lesion labels. Due to differences in acquisition parameters in the MSS3 compared with the images from the CVD dataset, in the MSS3 gray matter appears brighter relative to the white matter in the FLAIR images. This causes confusion for all models, with gray matter around the giri, insular cortex and caudate nucleus occasionally uncertain, and segmented as WMH in rare cases. However we note that SSN-Ens is substantially less prone to this behaviour, almost never segmenting gray matter and reporting less gray matter as highly uncertain, showing improved robustness to real world OOD scenarios (E.1a, E.1c).

Next we examine the identification of small WMH in the Challenge dataset (Figure 10b and Appendix F). While both models (i.e., SEnt and SSN-Ens) may fail to segment small WMH, SSN-Ens may identify whole clusters of unsegmented WMH in the uncertainty map (F.1b). Furthermore, SSN-Ens is more likely to highlight false positives in the segmentation as uncertain (F.1a, F.2b), while remaining confident in the centre of correctly segmented lesions. SEnt may however be highly uncertain among correctly segmented lesions (i.e SSN-Ens is not simply always more uncertain about a given region than SEnt). However, we find SSN-Ens reports low levels of uncertainty for some areas of gray matter where SEnt does not; this behaviour is specific to the differences in acquisition protocols and requires filtering out low level uncertainty values F.2d. Nonetheless, both models can silently fail (neither segment nor consider uncertain) some WMH.

Finally, examination of images with artefacts unseen during training from the ADNI dataset reveals model failures. Introduction of a bias field to the FLAIR image (Figure 11a) causes both methods to produce high levels of uncertainty around bright regions of the image while failing to detect WMH in darker regions of the image. The segmentations of both methods are highly asymmetrical compared to the WMH visible in FLAIR and SEnt introduces erroneous WMH between the ventricles. We further

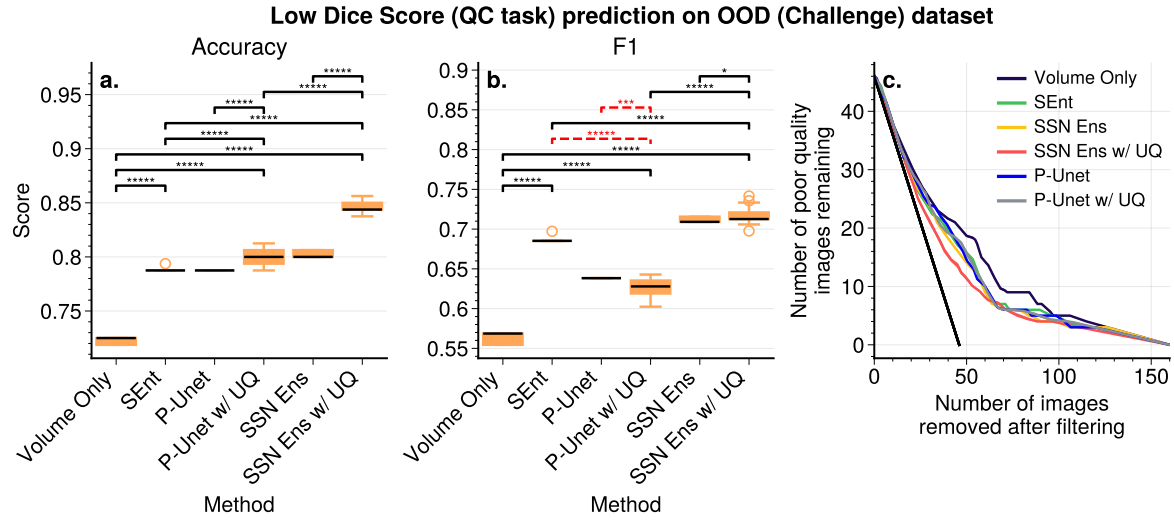


Figure (8) Results of the QC task. (a - b): For each technique, the plotted distribution shows the range of scores across all hyperparameter settings. The four methods are: Volume Only: prediction model using only the predicted WMH volume from the SEnt model. SEnt: Using spatial and regional volumetric features extracted from the WMH prediction from the SEnt model. SSN-Ens w/UQ: Using features extracted from both the WMH prediction, UQ map and distribution of features over multiple inferences for the SSN-Ens model. P-Unet w/UQ: Using features extracted from both the WMH prediction, UQ map and distribution of features over multiple inferences for the P-Unet model. Pairwise two-tailed t-test between each set of methods (comparing equivalent hyper-parameter choices between each method) **excluding** P-Unet and SSN Ens which are compared only to their variants with UQ features. Significance shown with ($p < 0.05$: *), ($p < 0.01$: **), ($p < 0.001$: ***), ($p < 0.0001$: ****), ($p < 0.00001$: *****). Black line/* denotes the right hand model shows significant improvement over left hand model; dotted red line/* denotes left hand model shows significant improvement over right hand model. If no line is shown, no significant pairwise relationship between methods is found. (c) Compares the number of poor quality images remaining vs the number of filtered images from the dataset as the probability threshold for detecting a poor quality image increases. Black line shows a perfect classifier.

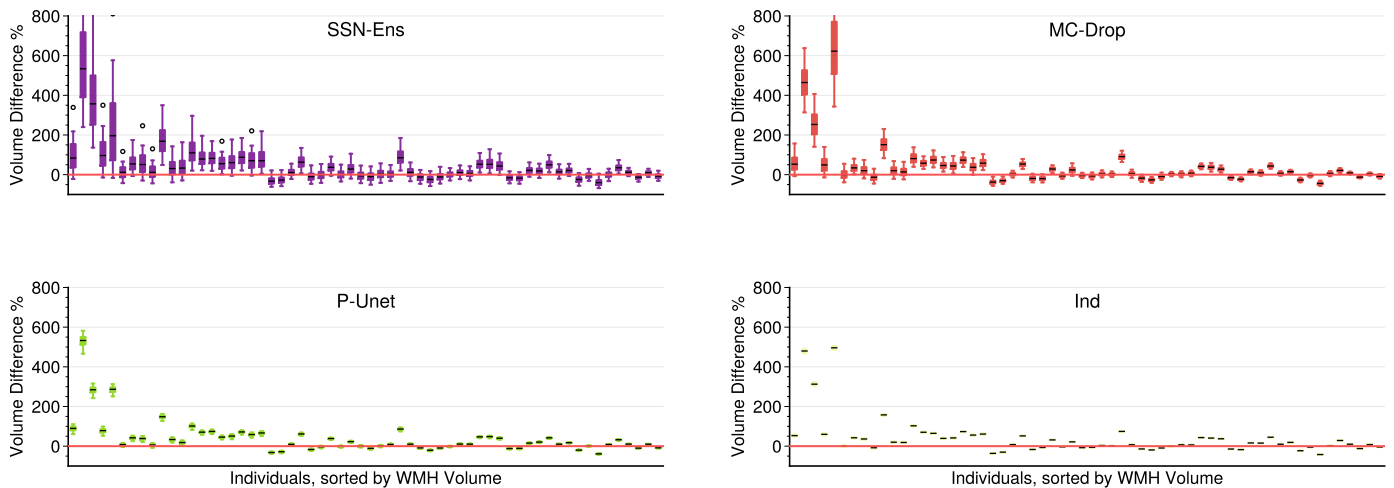
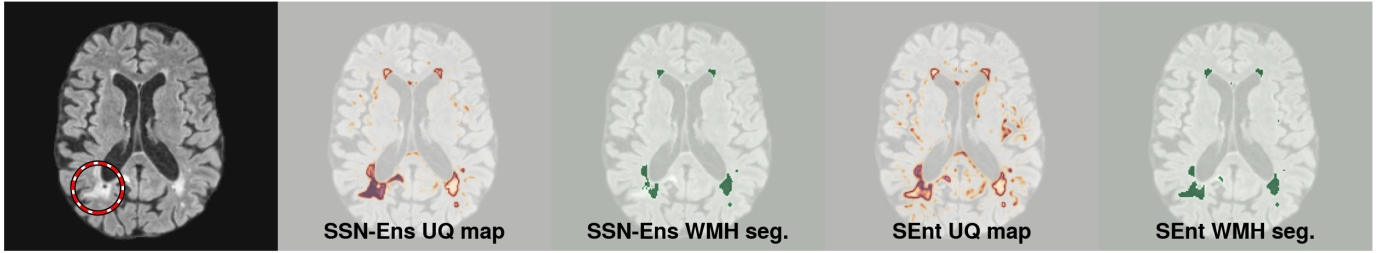
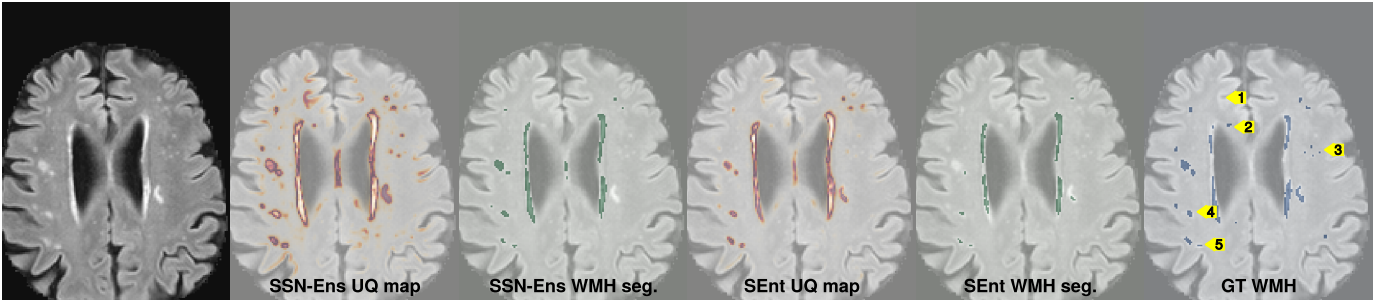


Figure (9) Volume Difference distribution of samples produced by (stochastic) methods on the OOD (Challenge) dataset. Individuals in the dataset are sorted in ascending order of ground truth WMH volume from left to right. Red Line indicates volume difference of 0 (i.e ground truth WMH volume).



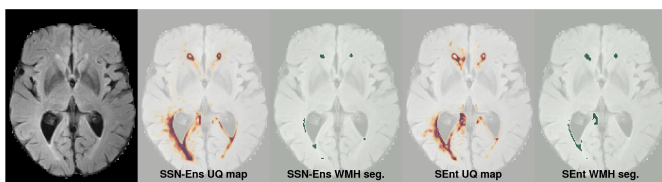
(a) **SEnt fails to identify a stroke lesion (segmented as WMH) as uncertain.** Red ring denotes known stroke lesion. While SSN-Ens segments part of the stroke lesion erroneously, the entire stroke lesion is identified as (highly) uncertain. SEnt only identifies the lesion boundary as uncertain, even when the stroke lesion deviates outside the spatial distribution of WMH. SEnt also highlights areas of the insular cortex as uncertain and partially segments this region, while SSN-Ens greatly reduces the uncertain area and does not segment the insular cortex.



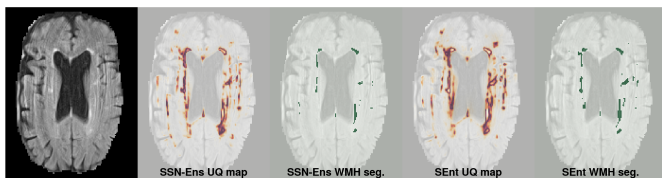
(b) **Arrow 1:** SSN-Ens introduces a number of areas of gray matter as uncertain in the image. **Arrow 2 and Arrow 3:** Both models fail to segment a number of small WMH clusters. However, SSN-Ens more consistently identifies these WMH as uncertain. **Arrow 4:** Both methods segment this WMH. However, the SEnt model is uncertain about the entire lesion. While this is not a failing of the uncertainty map, an ideal model will be certain in this case. The SSN-Ens model identifies only the boundary of this WMH as uncertain, and is confident in its prediction for the centre of the WMH. **Arrow 5:** The same as **Arrow 4**, for a cluster of two WMH. SSN-Ens highlights a number of gray matter areas as uncertain in this image.

Figure (10) Qualitative Analysis: examples from the (a) MSS3 and (b) Challenge datasets

find that in all cases where a visible head motion artefact is present (Figure 11b), UQ maps highlight the bright vertical streaks that overlap with the intensity distribution of WMH as uncertain. While the uncertainty map highlights the error, clearly a model that is robust to head motion and bias field is preferable, and modelling uncertainty alone is insufficient to achieve such robustness.



(a) Bias field present in FLAIR



(b) Severe head motion artefact

Figure (11) Comparison of failure cases on OOD data for the SSN-Ens and baseline SEnt models in the ADNI dataset. (a) Bias field in FLAIR. (b) Severe head motion.

5. Discussion

In this work we present four main contributions. Firstly, we benchmark uncertainty modelling techniques for semantic segmentation, finding that UQ improves WMH segmentation performance in both in-distribution and OOD data, and identifies areas where small WMH may have been missed. The combination of ensembles and stochastic segmentation networks (SSN-Ens) gives the strongest results, generalising robustly to unseen data. Secondly, we qualitatively examine the semantic information content of uncertainty maps from SSN-Ens compared to a baseline deterministic model (SEnt). SSN-Ens identifies stroke lesions within the spatial and volume distribution of WMH and identifies false negative WMH clusters as uncertain, while reducing the impact of some artefacts and acquisition parameter changes. This greatly improves over the baseline SEnt, which often misses entire WMH clusters in the deep white matter and can produce nonsensical or irrelevant uncertainty information. Thirdly, we propose an automated classification method for the Fazekas score using spatial and volumetric features from WMH segmentation and UQ maps. Spatial features significantly improve Fazekas classification performance over simple volume based estimation, and leveraging the increased robustness from UQ techniques such as P-Unet and SSN-Ens further boosts performance, with UQ map features providing significant improvements in performance for in-distribution data. Finally, we demonstrate that features

from SSN-Ens UQ maps enhance poor quality image detection, and that UQ techniques that yield high sample diversity can allow automation correction when WMH volume is overestimated in images from subjects with low WMH volume.

The implications of our findings are multifold. First, when comparing UQ techniques, it is important to consider more than one metric due to non-equivalent uncertainty thresholds between methods. Metrics such as AVD and sUEO vary considerably across subjects, so per-subject evaluation is key when choosing the right method for downstream tasks. For example, in a human-in-the-loop annotation setting where an annotator corrects uncertain voxels in the image P-UNet will be preferable due to its high UEO and PAVPU scores, while SSN-Ens will be preferable for accurate volume estimation and identification of all potential WMH lesions due to its high sample diversity and hence high WMH lesion coverage. Given the high aleatoric uncertainty inherent to WMH segmentation, and hence the high sample diversity required to capture the ‘ground truth’ segmentation within the predicted WMH distribution, D_{GED}^2 is dominated by the sample diversity term, which reduces the sUEO score. We found P-UNet is insufficiently expressive to capture all possible small WMH lesions, and adjusting the latent space size did not resolve this. Further techniques could improve P-UNet’s expressivity, for example: using normalizing flows (Valiuddin et al.), hierarchical latent spaces (Kohl et al., 2019) and using multivariate Gaussian mixtures (Bhat et al., 2022) or incorporating epistemic uncertainty (Hu et al., 2019). However such approaches increase the complexity of the method considerably compared to the SSN, which outperforms P-UNet with better quality in the distribution of WMH segmentations produced (e.g. lower D_{GED}^2 , higher Top Dice score).

Second, the assessment of the robustness of UQ techniques should be performed on realistic OOD data. Various works show that evidential deep learning may improve robustness (Amini et al., 2020; Zou et al., 2022, 2023b) while remaining computationally efficient. A common approach to demonstrate such robustness is via perturbations such as noise and augmentations, with similar approaches for MC-Drop (Mojiri Forooshani et al.). However, when using a separate real world OOD data, we find that performance improvements over the baseline from evidential deep learning (Evid) are limited compared to both MC-Drop and ensembling techniques, which achieve lower AVD and lesion coverage. Hence using OOD data to guide model choice is essential, as augmentations may not capture acquisition protocol, demographic and image quality variability. Furthermore, where robustness in terms of domain generalisation is considered the principal benefit of UQ, other UQ methods should not be the ultimate yardstick for method comparison, where arguably more appropriate baselines in the literature regarding robustness and domain generalisation are available (Lee et al., 2018), (Zhao et al., 2021).

Another popular approach for modelling aleatoric uncertainty is test time augmentation (TTA) (Wang et al., 2019), where multiple samples are generated by applying augmentations to an image before applying the model. While interpolations during augmentation may affect the delineation of the WMH boundaries, we conclude that intuitively the ambiguity around the presence of a small WMH (for example) should not depend on the typical augmentations used (such as rotations, rescaling and reflections). Hence we avoid comparing this type of methods in this work.

Third, UQ techniques capture semantically meaningful spatial information for informing the Fazekas classification task. Our proposed approach leveraging spatial and volumetric features across different brain regions clearly improves Fazekas score prediction over global WMH volume alone as it aligns naturally with neuroradiological interpretation guidelines. However, since Fazekas is generated directly from inspecting MRI images, factors such as the relative intensity of the normal appearing white matter (NAWM) in the WMH penumbra, marginally hyperintense regions or ambiguous small deep isolated WMH may contribute to differences in the SVD severity perceived by an annotator and hence the Fazekas score. Uncertainty maps help capture such regions, and uncertainty in the WMH penumbra that is anterior or posterior to the ventricle horn may give improved detection of potential confluence between Deep and PV regions. This may explain why UQ map features improve both model accuracy and calibration (lower RMBS score) in in-distribution data, as the model can express uncertainty among cases that are in-between Fazekas categories. However, we have demonstrated that evaluating the generalisability of Fazekas score classifiers in OOD data is potentially ill-posed due to the different criteria perceived in the annotation of each datasets and the lack of standards for generating consistent ground truth annotations that are amenable to probabilistic modelling. Where annotators use different criteria (policies) when providing annotations, this hinders cross-dataset comparison and can cause misleading results Philips et al. (2024). For example, in addition to the differences in volume distribution of each score between studies that we have demonstrated, a single small WMH cluster in the deep white matter may be considered by one annotator as sufficient for giving Fazekas DWMH score of 1 whilst another annotator might have chosen to give the score of 0. Hence, despite the known effectiveness of machine learning approaches, uniformity in the criteria for generating Fazekas scores, for example, based on a WMH segmentation agreed by annotators as gold standard, could allow for a clearer and interpretable link between the uncertainty in WMH and the downstream uncertainty in the Fazekas score. Despite the known floor and ceiling effects of the clinical visual scoring systems (Olsson et al., 2013; van Straaten et al.), effective automated Fazekas estimation could facilitate larger-scale research into WMH in clinical data.

Fourth, despite segmentation quality (e.g Dice score) depending heavily on WMH volume, we expect spatial features to improve QC prediction performance due to the increased difficulty in Deep WMH segmentation compared to the PV region. We would also expect that high uncertainty in a region may be indicative of low segmentation quality. However, the UQ features from P-Unet did not improve F1 score or filtering of low quality images. This suggests that the clear improvement in QC classification with SSN-Ens features is due to the high sample diversity and positive skew of the predicted WMH distribution among subjects where the median predicted WMH volume is greater than the ground truth, allowing identification of poor quality images.

There are many avenues for future research. Longitudinal analysis of uncertain regions in the NAWM could reveal meaningful biological information, such as regions of the normal appearing white matter that later develop into WMH, particularly around small isolated WMH.

Disentangling epistemic uncertainty from aleatoric uncertainty may allow for uncertainty information to be more effectively targeted at quality control and related tasks such as OOD detection which intuitively depend on epistemic uncertainty. However, disentangling epistemic from aleatoric uncertainty is a non-trivial task, as the conventional decomposition (Houlsby et al., 2011) of Shannon entropy (total uncertainty) into mutual information (epistemic uncertainty) and conditional entropy (aleatoric uncertainty) can yield inconsistent results in practice (Wimmer et al., 2023). Hence, in this work, we have chosen to evaluate the utility of the total uncertainty expressed by each technique without disentangling the epistemic component. However aleatoric uncertainty may not be informative for quality control tasks, while epistemic uncertainty due to artefacts, such as head motion, will impact the utility of UQ maps for other downstream tasks such as Fazekas prediction. This indicates that further separation of epistemic and aleatoric uncertainty is warranted.

The SSN-Ens method could be further improved in a number of ways. First, modelling the uncertainty over the logit space with other long tailed distributions, such as a low rank multivariate T distribution could further reduce the impact of noise during training (Gonzalez-Jimenez et al., 2023). Secondly, one hypothesis for the performance improvements on OOD (out-of-distribution) data attained with ensembles is due to ensemble diversity (de Mathelin et al., 2023). Hence, methods that attempt to improve the diversity of the ensemble have been pursued, demonstrating improvements in robustness and OOD detection (Mehrtens et al., 2022), (Zaidi et al., 2021), (D’Angelo et al., 2021). However, some argue this is explained due to differences in model capacity (Ovadia et al., 2019). Hence, further work comparing the effectiveness of SSN-Ens to other techniques that improve robustness to OOD data should be explored. Nonetheless, improving the diversity of the ensemble may be an effective way to boost robust-

ness and uncertainty representations. One way to do this, specific to WMH segmentation, may be to train individual ensemble elements on different datasets that cover a range of WMH segmentation policies (Philps et al., 2024), so that the full range of annotator disagreement (and thereby aleatoric uncertainty) can be accurately reflected by the model. However, complete sets of desired MRI acquisitions for applying a model (e.g FLAIR and T1w) are in general not available in clinical settings (Ruffle et al., 2023) and so assessing suitability for clinical settings needs to go beyond assessing OOD performance, for example by providing segmentation on available scans, whether it is T2, T2* or T1-CE for broad applicability. Finally, in order to move towards an automated neuroradiological support system for studying SVD in clinical patients, application of UQ and robust generalisation techniques to other neuroradiological markers of SVD in a multi-label setting, in particular for stroke lesions and perivascular spaces, is essential. This would not only improve stroke lesion detection but allow separation of uncertainty around WMH locations and size from uncertainty around pathology type, improving performance in downstream tasks such as Fazekas scoring.

Acknowledgements

We thank Simon R. Cox, Daniela Jaime Garcia, Junfang Zhang, Xiaodi Liu and Yajun Cheng for their contribution to the curation of datasets utilised in this work. BP was funded by the United Kingdom Research and Innovation Centre for Doctoral Training in Biomedical AI Programme scholarships (grant EP/S02431X/1). For the purpose of open access, the author has applied a creative commons attribution (CC BY) licence to any author accepted manuscript version arising. Funding from Row Fogo Charitable Trust (Ref No: AD.ROW4.35. BRO-D.FID3668413), and the UK Medical Research Council (UK Dementia Research Institute at the University of Edinburgh, award number UK DRI-4002;G0700704/84698) are also gratefully acknowledged. M.O.B. gratefully acknowledges funding from: Fondation Leducq Transatlantic Network of Excellence (17 CVD 03); EPSRC grant no. EP/X025705/1; British Heart Foundation and The Alan Turing Institute Cardiovascular Data Science Award (C-10180357); Diabetes UK (20/0006221); Fight for Sight (5137/5138); the SCONE projects funded by Chief Scientist Office, Edinburgh & Lothians Health Foundation, Sight Scotland, the Royal College of Surgeons of Edinburgh, the RS Macdonald Charitable Trust, and Fight For Sight; the Neurii initiative which is a partnership among Eisai Co., Ltd, Gates Ventures, LifeArc and HDR UK.

Data collection and sharing for the Alzheimer’s Disease Neuroimaging Initiative (ADNI) is funded by the National Institute on Aging (National Institutes of Health Grant U19 AG024904). The grantee organization is the Northern California Institute for Research and Education. In the past, ADNI has also received funding from the National Institute of Biomedical Imaging and Bioengineering,

the Canadian Institutes of Health Research, and private sector contributions through the Foundation for the National Institutes of Health (FNIH) including generous contributions from the following: AbbVie, Alzheimer’s Association; Alzheimer’s Drug Discovery Foundation; Araclon Biotech; BioClinica, Inc.; Biogen; Bristol-Myers Squibb Company; CereSpir, Inc.; Cogstate; Eisai Inc.; Elan Pharmaceuticals, Inc.; Eli Lilly and Company; EuroImmun; F. Hoffmann-La Roche Ltd and its affiliated company Genentech, Inc.; Fujirebio; GE Healthcare; IXICO Ltd.; Janssen Alzheimer Immunotherapy Research & Development, LLC.; Johnson & Johnson Pharmaceutical Research & Development LLC.; Lumosity; Lundbeck; Merck & Co., Inc.; Meso Scale Diagnostics, LLC.; NeuroRx Research; Neurotrack Technologies; Novartis Pharmaceuticals Corporation; Pfizer Inc.; Piramal Imaging; Servier; Takeda Pharmaceutical Company; and Transition Therapeutics.

References

Abdar, M., Pourpanah, F., Hussain, S., Rezazadegan, D., Liu, L., Ghavamzadeh, M., Fieguth, P., Cao, X., Khosravi, A., Acharya, U.R., Makarek, V., Nahavandi, S., . A review of uncertainty quantification in deep learning: Techniques, applications and challenges. *Information Fusion* 76, 243–297. URL: <https://www.sciencedirect.com/science/article/pii/S1566253521001081>, doi:10.1016/j.inffus.2021.05.008.

Abe, T., Buchanan, E.K., Pleiss, G., Zemel, R., Cunningham, J.P., 2022. Deep ensembles work, but are they necessary? *Advances in Neural Information Processing Systems* 35, 33646–33660.

Amini, A., Schwarting, W., Soleimany, A., Rus, D., 2020. Deep evidential regression. *Advances in Neural Information Processing Systems* 33, 14927–14937.

Andere, A., Jindal, G., Molino, J., Collins, S., Merck, D., Burton, T., Stretz, C., Yaghi, S., Sacchetti, D.C., Jamal, S.E., Reznik, M.E., Furie, K., Cutting, S., . Volumetric white matter hyperintensity ranges correspond to fazekas scores on brain MRI. *Journal of Stroke and Cerebrovascular Diseases* 31, 106333. URL: <https://www.sciencedirect.com/science/article/pii/S105230572200301>, doi:10.1016/j.jstrokecerebrovasdis.2022.106333.

Balakrishnan, R., Hernández, M.d.C.V., Farrall, A.J., 2021. Automatic segmentation of white matter hyperintensities from brain magnetic resonance images in the era of deep learning and big data—a systematic review. *Computerized Medical Imaging and Graphics* 88, 101867.

Barnett, M., Wang, D., Beadnall, H., Bischof, A., Brunacci, D., Butzkueven, H., Brown, J.W.L., Cabezas, M., Das, T., Dugal, T., Guilfoyle, D., Klistorner, A., Krieger, S., Kyle, K., Ly, L., Masters, L., Shieh, A., Tang, Z., van der Walt, A., Ward, K., Wiendl, H., Zhan, G., Zivadinov, R., Barnett, Y., Wang, C., . A real-world clinical validation for AI-based MRI monitoring in multiple sclerosis. *npj Digital Medicine* 6, 1–9. URL: <https://www.nature.com/articles/s41746-023-00940-6>, doi:10.1038/s41746-023-00940-6. publisher: Nature Publishing Group.

Begoli, E., Bhattacharya, T., Kusnezov, D., 2019. The need for uncertainty quantification in machine-assisted medical decision making. *Nature Machine Intelligence* 1, 20–23.

Bhat, I., Plum, J.P., Kuijff, H.J., 2022. Generalized probabilistic unet for medical image segmentation, in: *International Workshop on Uncertainty for Safe Utilization of Machine Learning in Medical Imaging*, Springer. pp. 113–124.

Billot, B., Greve, D.N., Puonti, O., Thielscher, A., Van Leemput, K., Fischl, B., Dalca, A.V., Iglesias, J.E., 2023. Syntheseg: Segmentation of brain MRI scans of any contrast and resolution without retraining. *Medical Image Analysis* 86, 102789. doi:10.1016/j.media.2023.102789.

Blei, D.M., Kucukelbir, A., McAuliffe, J.D., 2017. Variational inference: A review for statisticians. *Journal of the American statistical Association* 112, 859–877.

Blundell, C., Cornebise, J., Kavukcuoglu, K., Wierstra, D., 2015. Weight uncertainty in neural network, in: *International conference on machine learning*, PMLR. pp. 1613–1622.

Borchert, R.J., Azevedo, T., Badhwar, A., Bernal, J., Betts, M., Bruffaerts, R., Burkhart, M.C., Dewachter, I., Gellersen, H.M., Low, A., Lourida, I., Machado, L., Madan, C.R., Malpetti, M., Mejia, J., Michopoulou, S., Muñoz-Neira, C., Pepys, J., Peres, M., Phillips, V., Ramanan, S., Tamburin, S., Tantiangco, H.M., Thakur, L., Tomassini, A., Vipin, A., Tang, E., Newby, D., Network, T.D.D.P.D., Ranson, J.M., Llewellyn, D.J., Veldsman, M., Rittman, T., . Artificial intelligence for diagnostic and prognostic neuroimaging in dementia: A systematic review. *Alzheimer’s & Dementia* 19, 5885–5904. URL: <https://onlinelibrary.wiley.com/doi/abs/10.1002/alz.13412>, doi:10.1002/alz.13412. eprint: <https://onlinelibrary.wiley.com/doi/pdf/10.1002/alz.13412>.

Cedres, N., Ferreira, D., Machado, A., Shams, S., Sacuiu, S., Waern, M., Wahlund, L.O., Zettergren, A., Kern, S., Skoog, I., Westman, E., . Predicting fazekas scores from automatic segmentations of white matter signal abnormalities. *Aging (Albany NY)* 12, 894–901. URL: <https://www.ncbi.nlm.nih.gov/pmc/articles/PMC6977667/>, doi:10.18632/aging.102662.

Charpentier, B., Senanayake, R., Kochenderfer, M., Günnemann, S., 2022. Disentangling epistemic and aleatoric uncertainty in reinforcement learning. *arXiv preprint arXiv:2206.01558* .

Choi, K.S., Sunwoo, L., 2022. Artificial intelligence in neuroimaging: clinical applications. *Investigative Magnetic Resonance Imaging* 26, 1–9.

Clancy, U., Garcia, D.J., Stringer, M.S., Thrippleton, M.J., Valdés Hernández, M.d.C., Wiseman, S., Hamilton, O.K., Chappell, F.M., Brown, R., Blair, G.W., Hewins, W., Sleight, E., Ballerini, L., Bastin, M.E., Muñoz Maniega, S., MacGillivray, T., Hetherington, K., Hamid, C., Arteaga, C., Morgan, A.G., Manning, C., Backhouse, E., Hamilton, I., Job, D., Marshall, I., Doubal, F.N., Wardlaw, J.M., . Rationale and design of a longitudinal study of cerebral small vessel diseases, clinical and imaging outcomes in patients presenting with mild ischaemic stroke: Mild stroke study 3. *European Stroke Journal* 6, 81–88. URL: <https://doi.org/10.1177/2396987320929617>, doi:10.1177/2396987320929617. publisher: SAGE Publications.

Cuttillo, C.M., Sharma, K.R., Foschini, L., Kundu, S., Mackintosh, M., Mandl, K.D., 2020. Machine intelligence in healthcare—perspectives on trustworthiness, explainability, usability, and transparency. *NPJ digital medicine* 3, 1–5.

Czolbe, S., Arnavaz, K., Krause, O., Feragen, A., 2021. Is segmentation uncertainty useful?, in: *Information Processing in Medical Imaging: 27th International Conference, IPMI 2021, Virtual Event, June 28–June 30, 2021, Proceedings 27*, Springer. pp. 715–726.

D’Angelo, F., Fortuin, V., Wenzel, F., 2021. On stein variational neural network ensembles. *arXiv preprint arXiv:2106.10760* .

DeBette, S., Markus, H., 2010. The clinical importance of white matter hyperintensities on brain magnetic resonance imaging: systematic review and meta-analysis. *Bmj* 341.

Ding, T., Cohen, A., O’Connor, E., Karim, H., Crainiceanu, A., Muschelli, J., Lopez, O., Klunk, W., Aizenstein, H., Krafty, R., Crainiceanu, C., Tudorascu, D., . An improved algorithm of white matter hyperintensity detection in elderly adults. *NeuroImage: Clinical* 25, 102151. URL: <https://www.sciencedirect.com/science/article/pii/S2213158219304978>, doi:10.1016/j.nicl.2019.102151.

Fazekas, F., Chawluk, J.B., Alavi, A., Hurtig, H.I., Zimmerman, R.A., 1987. Mr signal abnormalities at 1.5 t in alzheimer’s dementia and normal aging. *American Journal of Neuroradiology* 8, 421–426.

Gal, Y., Ghahramani, Z., 2016. Dropout as a bayesian approximation: Representing model uncertainty in deep learning, in: *international conference on machine learning*, PMLR. pp. 1050–1059.

- Ganaie, M.A., Hu, M., Malik, A., Tanveer, M., Suganthan, P., 2022. Ensemble deep learning: A review. *Engineering Applications of Artificial Intelligence* 115, 105151.
- Gao, C., McGilchrist, M., Mumtaz, S., Hall, C., Anderson, L.A., Zurowski, J., Gordon, S., Lumsden, J., Munro, V., Wozniak, A., Sibley, M., Banks, C., Duncan, C., Linksted, P., Hume, A., Stables, C.L., Mayor, C., Caldwell, J., Wilde, K., Cole, C., Jefferson, E., . A national network of safe havens: Scottish perspective. *Journal of Medical Internet Research* 24, e31684. URL: <https://www.jmir.org/2022/3/e31684>, doi:10.2196/31684. company: Journal of Medical Internet Research Distributor: Journal of Medical Internet Research Institution: Journal of Medical Internet Research Label: Journal of Medical Internet Research Publisher: JMIR Publications Inc., Toronto, Canada.
- Gonzalez-Jimenez, A., Lionetti, S., Gottfrois, P., Gröger, F., Pouly, M., Navarini, A.A., 2023. Robust t-loss for medical image segmentation, in: *International Conference on Medical Image Computing and Computer-Assisted Intervention*, Springer. pp. 714–724.
- Gootjes, L., Teipel, S., Zebuhr, Y., Schwarz, R., Leinsinger, G., Scheltens, P., Möller, H.J., Hampel, H., 2004. Regional distribution of white matter hyperintensities in vascular dementia, alzheimer's disease and healthy aging. *Dementia and geriatric cognitive disorders* 18, 180–188.
- Griffanti, L., Jenkinson, M., Suri, S., Zsoldos, E., Mahmood, A., Filippini, N., Sexton, C.E., Topiwala, A., Allan, C., Kivimäki, M., Singh-Manoux, A., Ebmeier, K.P., Mackay, C.E., Zamboni, G., . Classification and characterization of periventricular and deep white matter hyperintensities on MRI: A study in older adults. *NeuroImage* 170, 174–181. URL: <https://www.sciencedirect.com/science/article/pii/S1053811917302318>, doi:10.1016/j.neuroimage.2017.03.024.
- Gronewold, J., Jokisch, M., Schramm, S., Himpfen, H., Ginster, T., Tenhagen, I., Doeppner, T.R., Jockwitz, C., Miller, T., Lehmann, N., Moebus, S., Jöckel, K.H., Erbel, R., Caspers, S., Hermann, D.M., . Periventricular rather than deep white matter hyperintensities mediate effects of hypertension on cognitive performance in the population-based 1000brains study. *Journal of Hypertension* 40, 2413. URL: https://journals.lww.com/jhypertension/fulltext/2022/12000/Periventricular_rather_than_deep_white_matter.8.aspx, doi:10.1097/HJH.0000000000003270.
- Guerrero, R., Qin, C., Oktay, O., Bowles, C., Chen, L., Joules, R., Wolz, R., Valdés-Hernández, M.C., Dickie, D.A., Wardlaw, J., Rueckert, D., . White matter hyperintensity and stroke lesion segmentation and differentiation using convolutional neural networks. *NeuroImage: Clinical* 17, 918–934. URL: <https://www.sciencedirect.com/science/article/pii/S2213158217303273>, doi:10.1016/j.nicl.2017.12.022.
- Guo, X., Ye, C., Yang, Y., Zhang, L., Liang, L., Lu, S., Lv, H., Guo, C., Ma, T., 2022. Ensemble learning via supervision augmentation for white matter hyperintensity segmentation. *Frontiers in Neuroscience* 16. URL: <http://dx.doi.org/10.3389/fnins.2022.946343>, doi:10.3389/fnins.2022.946343.
- Han, Z., Zhang, C., Fu, H., Zhou, J.T., 2022. Trusted multi-view classification with dynamic evidential fusion. *IEEE transactions on pattern analysis and machine intelligence* 45, 2551–2566.
- Harper, A.M., Clayson, L., Wardlaw, J.M., Valdés Hernández, M.d.C., Initiative, A.D.N., 2018. Considerations on accuracy, pattern and possible underlying factors of brain microbleed progression in older adults with absence or mild presence of vascular pathology. *Journal of International Medical Research* 46, 3518–3538.
- Harrison, J., Willes, J., Snoek, J., 2024. Variational bayesian last layers. *arXiv preprint arXiv:2404.11599* .
- Hellström, M., Löfstedt, T., Garpebring, A., 2023. Denoising and uncertainty estimation in parameter mapping with approximate bayesian deep image priors. *Magnetic Resonance in Medicine* 90, 2557–2571.
- Houlsby, N., Huszár, F., Ghahramani, Z., Lengyel, M., 2011. Bayesian active learning for classification and preference learning. *arXiv preprint arXiv:1112.5745* .
- Hu, S., Worrall, D., Knecht, S., Veeling, B., Huisman, H., Welling, M., 2019. Supervised uncertainty quantification for segmentation with multiple annotations, in: *International Conference on Medical Image Computing and Computer-Assisted Intervention*, Springer. pp. 137–145.
- Iglesias, J.E., Liu, C.Y., Thompson, P.M., Tu, Z., 2011. Robust brain extraction across datasets and comparison with publicly available methods. *IEEE transactions on medical imaging* 30, 1617–1634.
- Isensee, F., Jaeger, P.F., Kohl, S.A., Petersen, J., Maier-Hein, K.H., 2021. nnu-net: a self-configuring method for deep learning-based biomedical image segmentation. *Nature methods* 18, 203–211.
- Jiménez-Balado, J., Corlier, F., Habeck, C., Stern, Y., Eich, T., 2022. Effects of white matter hyperintensities distribution and clustering on late-life cognitive impairment. *Scientific reports* 12, 1955.
- Joo, L., Shim, W.H., Suh, C.H., Lim, S.J., Heo, H., Kim, W.S., Hong, E., Lee, D., Sung, J., Lim, J.S., Lee, J.H., Kim, S.J., 2022. Diagnostic performance of deep learning-based automatic white matter hyperintensity segmentation for classification of the fazekas scale and differentiation of subcortical vascular dementia. *PLOS ONE* 17, e0274562. URL: <http://dx.doi.org/10.1371/journal.pone.0274562>, doi:10.1371/journal.pone.0274562.
- Joy, T.T., Sedai, S., Garnavi, R., 2021. Analyzing epistemic and aleatoric uncertainty for drusen segmentation in optical coherence tomography images. *arXiv preprint arXiv:2101.08888* .
- Jungo, A., Balsiger, F., Reyes, M., 2020. Analyzing the quality and challenges of uncertainty estimations for brain tumor segmentation. *Frontiers in neuroscience* 14, 282.
- Kendall, A., Gal, Y., 2017. What uncertainties do we need in bayesian deep learning for computer vision? *Advances in neural information processing systems* 30.
- Kim, K.W., MacFall, J.R., Payne, M.E., 2008. Classification of white matter lesions on magnetic resonance imaging in elderly persons. *Biological psychiatry* 64, 273–280.
- Kohl, S., Romera-Paredes, B., Meyer, C., De Fauw, J., Ledsam, J.R., Maier-Hein, K., Eslami, S., Jimenez Rezende, D., Ronneberger, O., 2018. A probabilistic u-net for segmentation of ambiguous images. *Advances in neural information processing systems* 31.
- Kohl, S.A., Romera-Paredes, B., Maier-Hein, K.H., Rezende, D.J., Eslami, S., Kohli, P., Zisserman, A., Ronneberger, O., 2019. A hierarchical probabilistic u-net for modeling multi-scale ambiguities. *arXiv preprint arXiv:1905.13077* .
- Kuijff, H.J., Biesbroek, J.M., De Bresser, J., Heinen, R., Andermatt, S., Bento, M., Berseth, M., Belyaev, M., Cardoso, M.J., Casamitjana, A., Collins, D.L., Dadar, M., Georgiou, A., Ghafoorian, M., Jin, D., Khademi, A., Knight, J., Li, H., Lladó, X., Luna, M., Mahmood, Q., McKinley, R., Mehrtash, A., Ourselin, S., Park, B.Y., Park, H., Park, S.H., Pezold, S., Puybareau, E., Rittner, L., Sudre, C.H., Valverde, S., Vilaplana, V., Wiest, R., Xu, Y., Xu, Z., Zeng, G., Zhang, J., Zheng, G., Chen, C., van der Flier, W., Barkhof, F., Viergever, M.A., Biessels, G.J., . Standardized assessment of automatic segmentation of white matter hyperintensities and results of the WMH segmentation challenge. *IEEE Transactions on Medical Imaging* 38, 2556–2568. URL: <https://ieeexplore.ieee.org/abstract/document/8669968>, doi:10.1109/TMI.2019.2905770. conference Name: IEEE Transactions on Medical Imaging.
- Lakshminarayanan, B., Pritzel, A., Blundell, C., 2017. Simple and scalable predictive uncertainty estimation using deep ensembles. *Advances in neural information processing systems* 30.
- Lambert, B., Forbes, F., Doyle, S., Dehaene, H., Dojat, M., 2024. Trustworthy clinical ai solutions: a unified review of uncertainty quantification in deep learning models for medical image analysis. *Artificial Intelligence in Medicine* , 102830.
- Laves, M.H., Tölle, M., Ortmaier, T., 2020. Uncertainty estimation in medical image denoising with bayesian deep image prior, in: *Uncertainty for Safe Utilization of Machine Learning in Medical Imaging, and Graphs in Biomedical Image Analysis: Second International Workshop, UNSURE 2020, and Third International Workshop, GRAIL 2020, Held in Conjunction with MICCAI 2020, Lima, Peru, October 8, 2020, Proceedings 2*, Springer. pp. 81–96.
- Lee, K., Lee, K., Lee, H., Shin, J., 2018. A simple unified framework

- for detecting out-of-distribution samples and adversarial attacks. Advances in neural information processing systems 31.
- Lee, S., Purushwalkam, S., Cogswell, M., Crandall, D., Batra, D., 2015. Why m heads are better than one: Training a diverse ensemble of deep networks. arXiv preprint arXiv:1511.06314 .
- Leming, M.J., Bron, E.E., Bruffaerts, R., Ou, Y., Iglesias, J.E., Golub, R.L., Im, H., 2023. Challenges of implementing computer-aided diagnostic models for neuroimages in a clinical setting. NPJ Digital Medicine 6, 129.
- Li, B., Qi, P., Liu, B., Di, S., Liu, J., Pei, J., Yi, J., Zhou, B., 2023a. Trustworthy ai: From principles to practices. ACM Computing Surveys 55, 1–46.
- Li, H., Nan, Y., Del Ser, J., Yang, G., 2022. Region-based evidential deep learning to quantify uncertainty and improve robustness of brain tumor segmentation. arXiv preprint arXiv:2208.06038 .
- Li, H., Nan, Y., Del Ser, J., Yang, G., 2023b. Region-based evidential deep learning to quantify uncertainty and improve robustness of brain tumor segmentation. Neural Computing and Applications 35, 22071–22085.
- Liang, W., Tadesse, G.A., Ho, D., Fei-Fei, L., Zaharia, M., Zhang, C., Zou, J., 2022. Advances, challenges and opportunities in creating data for trustworthy ai. Nature Machine Intelligence 4, 669–677.
- Lim, Z.W., Lee, M.L., Hsu, W., Wong, T.Y., 2019. Building trust in deep learning system towards automated disease detection, in: Proceedings of the AAAI Conference on Artificial Intelligence, pp. 9516–9521.
- Litjens, G., Kooi, T., Bejnordi, B.E., Setio, A.A.A., Ciompi, F., Ghafoorian, M., Van Der Laak, J.A., Van Ginneken, B., Sánchez, C.I., 2017. A survey on deep learning in medical image analysis. Medical image analysis 42, 60–88.
- Liu, J.Z., Padhy, S., Ren, J., Lin, Z., Wen, Y., Jerfel, G., Nado, Z., Snoek, J., Tran, D., Lakshminarayanan, B., 2023. A simple approach to improve single-model deep uncertainty via distance-awareness. J. Mach. Learn. Res. 24, 42–1.
- Lowekamp, B.C., Chen, D.T., Ibáñez, L., Blezek, D., 2013. The design of simpleitk. Frontiers in neuroinformatics 7, 45.
- Maillard, P., Fletcher, E., Harvey, D., Carmichael, O., Reed, B., Mungas, D., DeCarli, C., 2011. White matter hyperintensity penumbra. Stroke 42, 1917–1922.
- de Mathelin, A., Deheeger, F., Mougeot, M., Vayatis, N., 2023. Deep anti-regularized ensembles provide reliable out-of-distribution uncertainty quantification. arXiv preprint arXiv:2304.04042 .
- Mehrtens, H.A., Gonzalez, C., Mukhopadhyay, A., 2022. Improving robustness and calibration in ensembles with diversity regularization, in: DAGM German Conference on Pattern Recognition, Springer. pp. 36–50.
- Mojiri Forooshani, P., Biparva, M., Ntiri, E.E., Ramirez, J., Boone, L., Holmes, M.F., Adamo, S., Gao, F., Ozzoude, M., Scott, C.J.M., Dowlatshahi, D., Lawrence-Dewar, J.M., Kwan, D., Lang, A.E., Marcotte, K., Leonard, C., Rochon, E., Heyn, C., Bartha, R., Strother, S., Tardif, J.C., Symons, S., Masellis, M., Swartz, R.H., Moody, A., Black, S.E., Goubran, M., . Deep bayesian networks for uncertainty estimation and adversarial resistance of white matter hyperintensity segmentation. Human Brain Mapping 43, 2089–2108. URL: <https://onlinelibrary.wiley.com/doi/abs/10.1002/hbm.25784>, doi:10.1002/hbm.25784. eprint: <https://onlinelibrary.wiley.com/doi/pdf/10.1002/hbm.25784>.
- Molchanova, N., Raina, V., Malinin, A., Rosa, F.L., Depeursinge, A., Gales, M., Granziera, C., Müller, H., Graziani, M., Cuadra, M.B., 2025. Structural-based uncertainty in deep learning across anatomical scales: Analysis in white matter lesion segmentation. Computers in Biology and Medicine 184, 109336. URL: <http://dx.doi.org/10.1016/j.combiomed.2024.109336>, doi:10.1016/j.combiomed.2024.109336.
- Monsour, R., Dutta, M., Mohamed, A.Z., Borkowski, A., Viswanathan, N.A., 2022. Neuroimaging in the era of artificial intelligence: current applications. Federal Practitioner 39, S14.
- Monteiro, M., Le Folgoc, L., Coelho de Castro, D., Pawlowski, N., Marques, B., Kamnitsas, K., van der Wilk, M., Glocker, B., 2020. Stochastic segmentation networks: Modelling spatially correlated aleatoric uncertainty. Advances in Neural Information Processing Systems 33, 12756–12767.
- mu, s., Lu, W., Yu, G., Zheng, L., Qiu, J., 2023. Deep learning-based grading of white matter hyperintensities enables identification of potential markers in multi-sequence mri data URL: <http://dx.doi.org/10.2139/ssrn.4394492>, doi:10.2139/ssrn.4394492.
- Mukhoti, J., van Amersfoort, J., Torr, P.H., Gal, Y., 2021a. Deep deterministic uncertainty for semantic segmentation. arXiv preprint arXiv:2111.00079 .
- Mukhoti, J., Gal, Y., . Evaluating bayesian deep learning methods for semantic segmentation. URL: <http://arxiv.org/abs/1811.12709>, doi:10.48550/arXiv.1811.12709, arXiv:1811.12709.
- Mukhoti, J., Kirsch, A., van Amersfoort, J., Torr, P.H., Gal, Y., 2021b. Deterministic neural networks with inductive biases capture epistemic and aleatoric uncertainty. arXiv preprint arXiv:2102.11582 .
- Mukhoti, J., Kirsch, A., van Amersfoort, J., Torr, P.H., Gal, Y., 2023. Deep deterministic uncertainty: A new simple baseline, in: Proceedings of the IEEE/CVF Conference on Computer Vision and Pattern Recognition, pp. 24384–24394.
- Nenning, K.H., Langa, G., 2022. Machine learning in neuroimaging: from research to clinical practice. Die Radiologie 62, 1–10.
- Oda, M., Zheng, T., Hayashi, Y., Otake, Y., Hashimoto, M., Akashi, T., Aoki, S., Mori, K., 2021. Covid-19 infection segmentation from chest ct images based on scale uncertainty, in: Clinical Image-Based Procedures, Distributed and Collaborative Learning, Artificial Intelligence for Combating COVID-19 and Secure and Privacy-Preserving Machine Learning. Springer, pp. 88–97.
- Olsson, E., Klasson, N., Berge, J., Eckerström, C., Edman, Å., Malmgren, H., Wallin, A., 2013. White matter lesion assessment in patients with cognitive impairment and healthy controls: reliability comparisons between visual rating, a manual, and an automatic volumetric mri method—the gothenburg mci study. Journal of Aging Research 2013, 198471.
- Ovadia, Y., Fertig, E., Ren, J., Nado, Z., Sculley, D., Nowozin, S., Dillon, J., Lakshminarayanan, B., Snoek, J., 2019. Can you trust your model’s uncertainty? evaluating predictive uncertainty under dataset shift. Advances in neural information processing systems 32.
- Park, G., Hong, J., Duffy, B.A., Lee, J.M., Kim, H., 2021. White matter hyperintensities segmentation using the ensemble u-net with multi-scale highlighting foregrounds. Neuroimage 237, 118140.
- Philps, B., del C. Valdes Hernandez, M., Munoz Maniega, S., Bastin, M.E., Sakka, E., Clancy, U., Wardlaw, J.M., Bernabeu, M.O., 2024. Stochastic uncertainty quantification techniques fail to account for inter-analyst variability in white matter hyperintensity segmentation, in: Annual Conference on Medical Image Understanding and Analysis, Springer. pp. 34–53.
- Philps, B., Valdes Hernandez, M.d.C., Bernabeu Llinares, M., 2023. Proper scoring loss functions are simple and effective for uncertainty quantification of white matter hyperintensities, in: International Workshop on Uncertainty for Safe Utilization of Machine Learning in Medical Imaging, Springer. pp. 208–218.
- Rachmadi, M.F., Valdés-Hernández, M.d.C., Makin, S., Wardlaw, J., Komura, T., 2020. Automatic spatial estimation of white matter hyperintensities evolution in brain mri using disease evolution predictor deep neural networks. Medical image analysis 63, 101712.
- Rahman, T., Khandakar, A., Qiblawey, Y., Tahir, A., Kiranyaz, S., Abul Kashem, S.B., Islam, M.T., Al Maadeed, S., Zughaiier, S.M., Khan, M.S., Chowdhury, M.E.H., . Exploring the effect of image enhancement techniques on COVID-19 detection using chest x-ray images. Computers in Biology and Medicine 132, 104319. URL: <https://www.sciencedirect.com/science/article/pii/S001048252100113X>, doi:10.1016/j.combiomed.2021.104319.
- Reinhold, J.C., Dewey, B.E., Carass, A., Prince, J.L., 2019. Evaluating the impact of intensity normalization on mr image synthesis, in: Medical Imaging 2019: Image Processing, SPIE. pp. 890–898.
- Ruffle, J.K., Mohinta, S., Gray, R., Hyare, H., Nachev, P., 2023. Brain tumour segmentation with incomplete imaging data. Brain Communications 5, fcad118.
- S, P.T., Fleuret, F., . Uncertainty reduction for model adaptation in

- semantic segmentation, in: Proceedings of the IEEE/CVF Conference on Computer Vision and Pattern Recognition, pp. 9613–9623. URL: https://openaccess.thecvf.com/content/CVPR2021/html/S_Uncertainty_Reduction_for_Model_Adaptation_in_Semantic_Segmentation_CVPR_2021_paper.html?ref=https://githubhelp.com.
- Sensoy, M., Kaplan, L., Kandemir, M., 2018. Evidential deep learning to quantify classification uncertainty. *Advances in neural information processing systems* 31.
- Seoni, S., Jahmunah, V., Salvi, M., Barua, P.D., Molinari, F., Acharya, U.R., 2023. Application of uncertainty quantification to artificial intelligence in healthcare: A review of last decade (2013–2023). *Computers in Biology and Medicine*, 107441.
- Srivastava, N., Hinton, G., Krizhevsky, A., Sutskever, I., Salakhutdinov, R., 2014. Dropout: a simple way to prevent neural networks from overfitting. *The journal of machine learning research* 15, 1929–1958.
- van Straaten, E.C., Fazekas, F., Rostrup, E., Scheltens, P., Schmidt, R., Pantoni, L., Inzitari, D., Waldemar, G., Erkinjuntti, T., Mäntylä, R., Wahlund, L.O., Barkhof, F., . Impact of white matter hyperintensities scoring method on correlations with clinical data. *Stroke* 37, 836–840. URL: <https://www.ahajournals.org/doi/full/10.1161/01.STR.0000202585.26325.74>, doi:10.1161/01.STR.0000202585.26325.74. publisher: American Heart Association.
- Székel, G.J., Rizzo, M.L., 2013. Energy statistics: A class of statistics based on distances. *Journal of statistical planning and inference* 143, 1249–1272.
- Taghanaki, S.A., Zheng, Y., Zhou, S.K., Georgescu, B., Sharma, P., Xu, D., Comaniciu, D., Hamarneh, G., 2019. Combo loss: Handling input and output imbalance in multi-organ segmentation. *Computerized Medical Imaging and Graphics* 75, 24–33.
- Tanno, R., Worrall, D.E., Kaden, E., Ghosh, A., Grussu, F., Bizzi, A., Sotiropoulos, S.N., Criminisi, A., Alexander, D.C., 2021. Uncertainty modelling in deep learning for safer neuroimage enhancement: Demonstration in diffusion mri. *NeuroImage* 225, 117366. URL: <http://dx.doi.org/10.1016/j.neuroimage.2020.117366>, doi:10.1016/j.neuroimage.2020.117366.
- Ulmer, D., 2021. A survey on evidential deep learning for single-pass uncertainty estimation. arXiv preprint arXiv:2110.03051 .
- Ulmer, D.T., Hardmeier, C., Frelsen, J., . Prior and posterior networks: A survey on evidential deep learning methods for uncertainty estimation. *Transactions on Machine Learning Research* URL: <https://openreview.net/forum?id=xqS8k9E75c>.
- Valdés Hernández, M.d.C., Morris, Z., Dickie, D.A., Royle, N.A., Muñoz Maniega, S., Aribisala, B.S., Bastin, M.E., Deary, I.J., Wardlaw, J.M., 2012. Close correlation between quantitative and qualitative assessments of white matter lesions. *Neuroepidemiology* 40, 13–22.
- Valdés Hernández, M.d.C., Piper, R.J., Bastin, M.E., Royle, N.A., Muñoz Maniega, S., Aribisala, B.S., Murray, C., Deary, I.J., Wardlaw, J.M., 2014. Morphologic, distributional, volumetric, and intensity characterization of periventricular hyperintensities. *American Journal of Neuroradiology* 35, 55–62.
- Valdés Hernández, M.d.C., Reid, S., Mikhael, S., Pernet, C., Initiative, A.D.N., 2018. Do 2-year changes in superior frontal gyrus and global brain atrophy affect cognition? *Alzheimer’s & Dementia: Diagnosis, Assessment & Disease Monitoring* 10, 706–716.
- Valdés Hernández, M.d.C., Ballerini, L., Glatz, A., Aribisala, B.S., Bastin, M.E., Dickie, D.A., Duarte Coello, R., Muñoz Maniega, S., Wardlaw, J.M., 2023. Step-by-step pipeline for segmenting enlarged perivascular spaces from 3d t2-weighted mri, 2018–2023. URL: <https://doi.org/10.7488/ds/7486>.
- Valiuddin, M.M.A., Viviers, C.G.A., van Sloun, R.J.G., de With, P.H.N., van der Sommen, F., . Improving aleatoric uncertainty quantification in multi-annotated medical image segmentation with normalizing flows, in: Sudre, C.H., Licandro, R., Baumgartner, C., Melbourne, A., Dalca, A., Hutter, J., Tanno, R., Abaci Turk, E., Van Leemput, K., Torrents Barrena, J., Wells, W.M., Macgowan, C. (Eds.), *Uncertainty for Safe Utilization of Machine Learning in Medical Imaging, and Perinatal Imaging, Placental and Preterm Image Analysis*, Springer International Publishing, pp. 75–88. doi:10.1007/978-3-030-87735-4_8.
- Van Horn, J.D., Toga, A.W., 2014. Human neuroimaging as a “big data” science. *Brain imaging and behavior* 8, 323–331.
- Wang, G., Li, W., Aertsen, M., Deprest, J., Ourselin, S., Vercauteren, T., 2019. Aleatoric uncertainty estimation with test-time augmentation for medical image segmentation with convolutional neural networks. *Neurocomputing* 338, 34–45.
- Wang, J., Zhou, Y., He, Y., Li, Q., Zhang, W., Luo, Z., Xue, R., Lou, M., 2022. Impact of different white matter hyperintensities patterns on cognition: a cross-sectional and longitudinal study. *NeuroImage: Clinical* 34, 102978.
- Wardlaw, J.M., Smith, E.E., Biessels, G.J., Cordonnier, C., Fazekas, F., Frayne, R., Lindley, R.I., O’Brien, J.T., Barkhof, F., Benavente, O.R., Black, S.E., Brayne, C., Breteler, M., Chabriat, H., DeCarli, C., Leeuw, F.E.d., Doubal, F., Duering, M., Fox, N.C., Greenberg, S., Hachinski, V., Kilimann, I., Mok, V., Oost-enbrugge, R.v., Pantoni, L., Speck, O., Stephan, B.C.M., Teipel, S., Viswanathan, A., Werring, D., Chen, C., Smith, C., Buchem, M.v., Norrving, B., Gorelick, P.B., Dichgans, M., . Neuroimaging standards for research into small vessel disease and its contribution to ageing and neurodegeneration. *The Lancet Neurology* 12, 822–838. URL: [https://www.thelancet.com/journals/lanneur/article/PIIS1474-4422\(13\)70124-8/fulltext](https://www.thelancet.com/journals/lanneur/article/PIIS1474-4422(13)70124-8/fulltext), doi:10.1016/S1474-4422(13)70124-8. publisher: Elsevier.
- Wardlaw, J.M., Valdés Hernández, M.C., Muñoz-Maniega, S., 2015. What are white matter hyperintensities made of? relevance to vascular cognitive impairment. *Journal of the American Heart Association* 4, e001140.
- Wimmer, L., Sale, Y., Hofman, P., Bischl, B., Hüllermeier, E., 2023. Quantifying aleatoric and epistemic uncertainty in machine learning: Are conditional entropy and mutual information appropriate measures?, in: *Uncertainty in Artificial Intelligence*, PMLR. pp. 2282–2292.
- Yeung, M., Rundo, L., Nan, Y., Sala, E., Schönlieb, C.B., Yang, G., 2023. Calibrating the dice loss to handle neural network overconfidence for biomedical image segmentation. *Journal of Digital Imaging* 36, 739–752.
- You, C., Dai, W., Min, Y., Staib, L., Duncan, J.S., 2023. Implicit anatomical rendering for medical image segmentation with stochastic experts. arXiv preprint arXiv:2304.03209 .
- Zaidi, S., Zela, A., Elsken, T., Holmes, C.C., Hutter, F., Teh, Y., 2021. Neural ensemble search for uncertainty estimation and dataset shift. *Advances in Neural Information Processing Systems* 34, 7898–7911.
- Zhang, Y., Brady, M., Smith, S., 2001. Segmentation of brain mr images through a hidden markov random field model and the expectation-maximization algorithm. *IEEE transactions on medical imaging* 20, 45–57.
- Zhao, X., Sicilia, A., Minhas, D.S., O’Connor, E.E., Aizenstein, H.J., Klunk, W.E., Tudorascu, D.L., Hwang, S.J., 2021. Robust white matter hyperintensity segmentation on unseen domain, in: *2021 IEEE 18th International Symposium on Biomedical Imaging (ISBI)*, IEEE. pp. 1047–1051.
- Zou, K., Chen, Z., Yuan, X., Shen, X., Wang, M., Fu, H., 2023a. A review of uncertainty estimation and its application in medical imaging. arXiv preprint arXiv:2302.08119 .
- Zou, K., Yuan, X., Shen, X., Chen, Y., Wang, M., Goh, R.S.M., Liu, Y., Fu, H., 2023b. Evidencecap: Towards trustworthy medical image segmentation via evidential identity cap. arXiv preprint arXiv:2301.00349 .
- Zou, K., Yuan, X., Shen, X., Wang, M., Fu, H., 2022. Tbrats: Trusted brain tumor segmentation, in: *International Conference on Medical Image Computing and Computer-Assisted Intervention*, Springer. pp. 503–513.

Appendix A. CVD dataset test fold results

Table (A.1) (a) Mean Segmentation performance of each technique on the CVD dataset. Sample Dice/AVD refer to the best score attained from the 10 samples (forward inferences) generated from each model. (b) Uncertainty quality metrics for the CVD dataset. sUEO: Soft Uncertainty Error Overlap. D_{GED}^2 : Generalised energy distance. 95% confidence interval is calculated over the 6 model runs. Best results are shown in bold.

(a) Segmentation performance					(b) Uncertainty map performance		
	Dice	Top Dice	AVD%	Top AVD%	sUEO	D_{GED}^2	
SEnt	0.65 ± 0.02	—	30.7 ± 7.3	—	0.46 ± 0.01	—	
MC-Drop	0.67 ± 0.02	0.68 ± 0.02	28.5 ± 5.3	12.8 ± 3.9	0.46 ± 0.01	0.76 ± 0.04	
Ens	0.67 ± 0.02	0.68 ± 0.02	28.5 ± 5.4	11.1 ± 4.1	0.46 ± 0.01	0.69 ± 0.04	
Evid	0.67 ± 0.02	—	27.7 ± 6.7	—	0.47 ± 0.00	—	
Ind	0.67 ± 0.02	0.67 ± 0.02	28.3 ± 6.4	26.8 ± 6.2	0.47 ± 0.01	0.92 ± 0.05	
P-Unet	0.68 ± 0.02	0.68 ± 0.02	27.4 ± 5.5	21.7 ± 6.0	0.48 ± 0.01	0.89 ± 0.06	
SSN	0.68 ± 0.02	0.70 ± 0.02	28.9 ± 7.6	6.3 ± 2.4	0.45 ± 0.01	0.69 ± 0.04	
SSN-Ens	0.69 ± 0.02	0.70 ± 0.02	26.5 ± 5.7	4.9 ± 1.5	0.45 ± 0.01	0.63 ± 0.03	

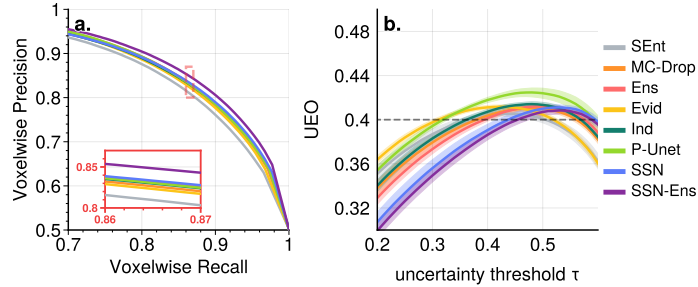


Figure (A.1) (a) Voxewise precision vs recall for WMH classification. Red box shows zoomed in view of the dashed region to demonstrate the ranking of method performance. (b) Mean Uncertainty error overlap (UEO) as τ changes. Dotted line shows UEO at 0.4.

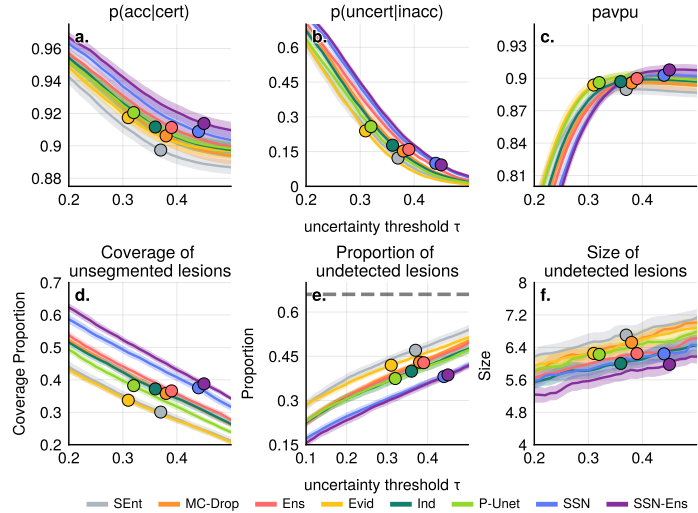


Figure (A.2) (a-c) Patchwise uncertainty metrics as τ changes for the OOD (Challenge) dataset. All metrics computed with a sliding window size of 4^3 voxels and accuracy threshold of 0.8. (a) Probability that a patch is accurate given that it is certain. (b) Probability that a patch is uncertain given that it is inaccurate. (c) PAvPU metric. (d-f) Lesion Instance Coverage metrics for the OOD (Challenge) dataset. Instances are 3D connected components in the ground truth WMH mask. (d) Coverage of unsegmented lesions: The mean proportion of unsegmented instances which are deemed uncertain. (e) Proportion of undetected lesions: The proportion of instances for which less than 50% of the instance (or less than 5 voxels, whichever is lower) are deemed uncertain and are segmented. Dashed line shows the number of instances which are undetected for baseline model SEnt in the WMH segmentation. Most instances are < 10 voxels in volume and undetected. (f) The size of undetected instances.

For all plots, the shaded area denotes the standard error over the 6 model runs, and the circles indicate the point at which each method attains an Uncertainty Error Overlap (UEO) of 0.4 on the CVD dataset.

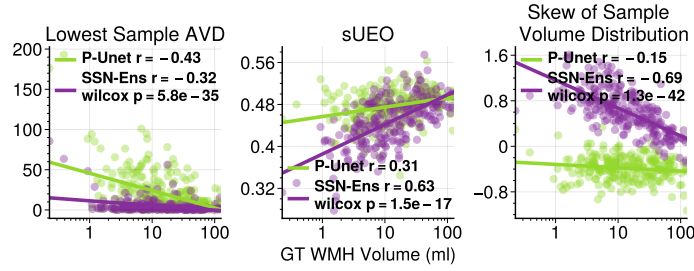


Figure (A.3) Comparison of P-Unet and SSN for each subject in the CVD dataset, reporting Pearson correlation coefficient and Wilcoxon signed-rank test. Lowest Sample AVD score: SSN-Ens exhibits consistently lower (better) top sample AVD score ($p = 5.8e - 35$) sUEO score: P-Unet exhibits consistently higher (better) soft Uncertainty Error Overlap (sUEO) score than SSN-Ens ($p = 1.5e - 17$).

Appendix B. Distribution of Dice scores for each cross-validation fold

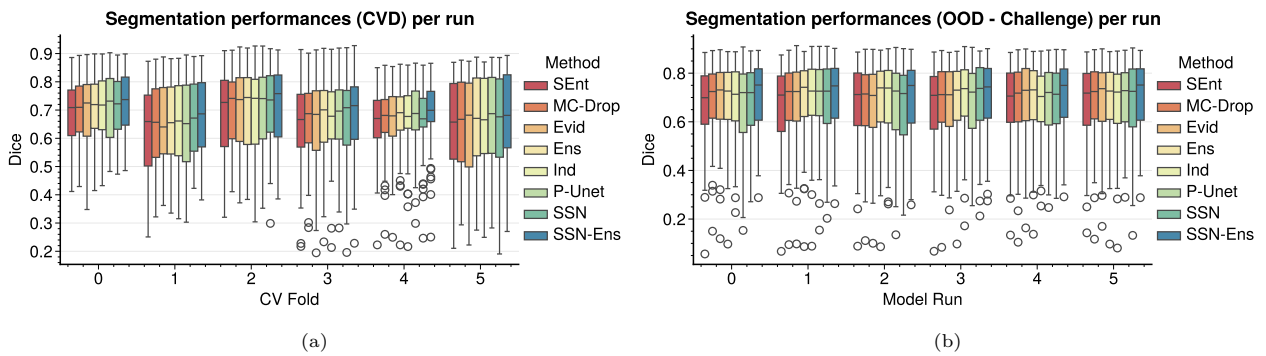


Figure (B.1) Distribution of Dice scores across individuals in the (a) CVD and (b) OOD (Challenge) dataset. (a) Models are trained using 6 fold cross validation, with each box and whisker plot showing the performance on the test split i for model i , $i \in 0..5$. (b) Each box and whisker plot i shows the performance of model i (originally trained on the CVD dataset)

Appendix C. Flair Intensity pre and post normalization

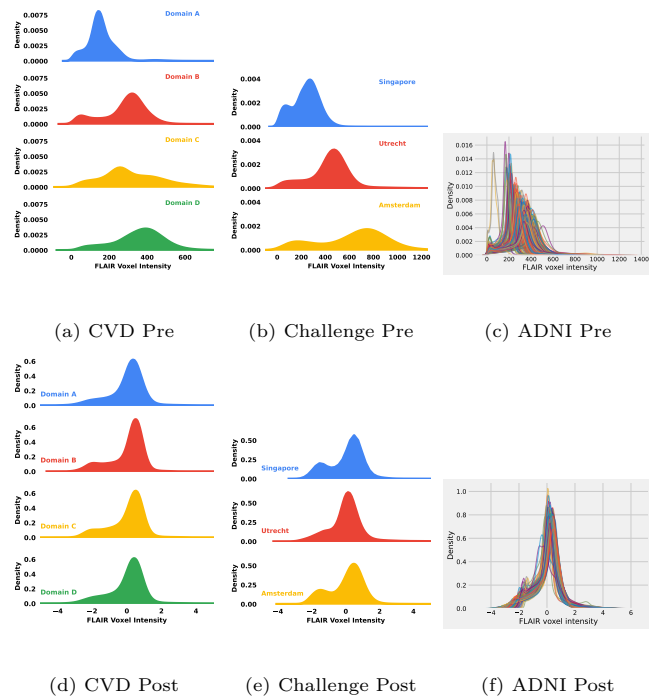


Figure (C.1) FLAIR voxel intensity distributions for all datasets pre and post Z-score normalization. For CVD and WMH Challenge datasets, we show a separate distribution for each domain, for ADNI we plot a distribution per image.

Appendix D. MRI Acquisition Parameters

Table (D.1) MRI parameters for each dataset.

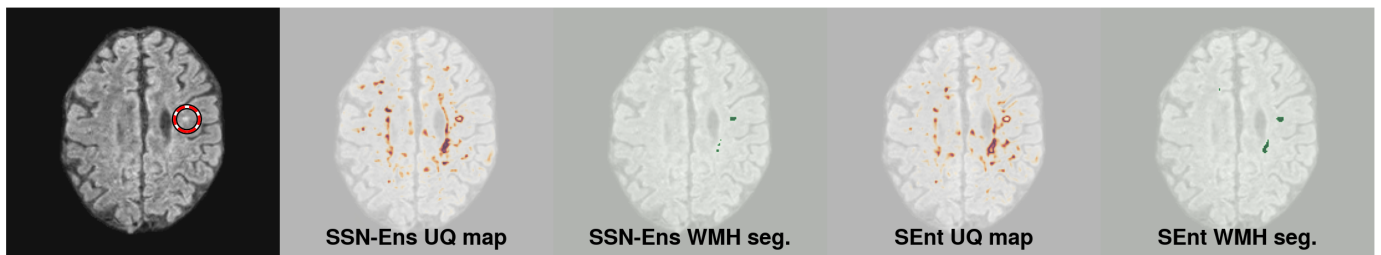
Dataset	Institute	Scanner	T1-weighted Voxel size (mm3)	TE/TR/TI (ms)	FLAIR Voxel size (mm3)	TE/TR/TI (ms)	Total
CVD	CCBS	1.5T GE Signa HDxt	0.9 × 0.9 × 6.5	9.0/ 440/ -	0.9 × 0.9 × 6.5	147/9002/ 2200	51
			0.5 × 0.5 × 4.0	4.0/ 9.6/ 500	0.5 × 0.5 × 4.0	100/8000/ 2000	25
			1.0 × 1.3 × 1.0	4.0/ 9.7/ 500	1.0 × 1.0 × 2.0	140/9000/ 2200	62
			1.0 × 0.9 × 1.0	4.0/ 9.7/ 500	0.5 × 0.5 × 6.0	140/9000/ 2200	112
MSS3	CCBS	3T Siemens Prisma	1.0 × 1.0 × 1.0	4.4/ 2500/ -	1.0 × 1.0 × 1.0	388/5000/ 1100	65
Chal.	UTC	3T Philips Achieva	1.0 × 1.0 × 1.0	4.5/ 7.9/ -	1.0 × 1.0 × 3.0	125/11000/ 2800	20/30
	SING	3T Siemens TrioTim	1.0 × 1.0 × 1.0	1.9/ 2300/ 900	1.0 × 1.0 × 3.0	82/9000/ 2500	20/30
	AMS	3T GE Signa HDxt	0.9 × 0.9 × 1.0	3.0/ 7.8/ -	1.0 × 1.0 × 1.2	126/8000/ 2340	20/30
	AMS	3T Philips Ingenuity	0.9 × 0.9 × 1.0	4.6/ 9.9/ -	1.0 × 1.0 × 0.6	279/8000/ 2340	0/10
	AMS	1.5T GE Signa HDxt	1.0 × 1.0 × 1.5	5.2/ 12.3/ -	1.2 × 1.2 × 1.3	117/6500/ 1987	0/10
ADNI	D1	3T Philips Intera	1.0 × 1.0 × 1.2	3.2/ 6.8/ -	0.9 × 0.9 × 5.0	90/9000/ 2500	16
	D2	3T Philips Intera	1.0 × 1.0 × 1.2	3.1/ 6.8/ -	0.9 × 0.9 × 5.0	90/9000/ 2500	3
	D3	3T Philips Ingenuia	1.0 × 1.0 × 1.2	3.2/ 6.8/ -	0.9 × 0.9 × 5.0	90/9000/ 2500	9
	D4	3T Philips Achieva	1.0 × 1.0 × 1.2	3.1/ 6.8/ -	0.9 × 0.9 × 5.0	90/9000/ 2500	34
	D5	3T Philips Achieva	1.0 × 1.0 × 1.2	3.2/ 6.8/ -	0.9 × 0.9 × 5.0	90/9000/ 2500	6
	D6	3T Philips Achieva	1.0 × 1.0 × 1.2	3.1/ 6.7/ -	0.9 × 0.9 × 5.0	90/9000/ 2500	10
	D7	3T Siemens Bio-graph mMR	1.0 × 1.0 × 1.2	3.0/ 2300/ 900	0.9 × 0.9 × 5.0	91/9000/ 2500	6
	D8	3T Siemens TrioTim	1.0 × 1.0 × 1.2	3.0/ 2300/ 900	0.9 × 0.9 × 5.0	90/9000/ 2500	127
	D9	3T Siemens TrioTim	1.1 × 1.1 × 1.2	3.0/ 2300/ 900	0.9 × 0.9 × 5.0	90/9000/ 2500	10
	D10	3T Siemens Skyra	1.0 × 1.0 × 1.2	3.0/ 2300/ 900	0.9 × 0.9 × 5.0	91/9000/ 2500	29
	D11	3T Siemens Skyra	1.1 × 1.0 × 1.2	3.0/ 2300/ 900	0.9 × 0.9 × 5.0	91/9000/ 2500	13
	D12	3T Siemens Verio	1.0 × 1.0 × 1.2	3.0/ 2300/ 900	0.9 × 0.9 × 5.0	91/9000/ 2500	32
	D13	3T GE Signa HDxt	1.0 × 1.0 × 1.2	3.0/ 7.0/ 400	0.9 × 0.9 × 5.0	154/11002/ 2250	2

Table D.1 lists the acquisition parameters for each dataset. All voxel sizes are given to the nearest 0.1mm while all TE/TR/TI times are given to the nearest 0.1ms. In the dataset column, Chal. refers to the OOD (Challenge) dataset. For the Challenge dataset, the Total column refers to (the number of images used in all evaluation metrics) / (the number of images used in the quality control experiment to predict the Dice score - see Section 3.7). For all other datasets, the Total column refers to the number of images included across all experiments. In the Institute column, for the CVD and MSS3 datasets, CCBS refers to Centre for Clinical Brain Sciences at The University of Edinburgh. For the Challenge dataset, UTC refers to University Medical Center Utrecht, SING refers to NUH Singapore and AMS refers to VU Amsterdam. For the ADNI dataset, the institute codes Dx(x) refer to the following ADNI centres: [**D1**: 002; **D2**: 053; **D3**: 006; **D4**: 010, 018, 019, 031, 100; **D5**: 012; **D6**: 130; **D7**: 013; **D8**: 011, 014, 022, 023, 024, 032, 035, 041, 073, 082, 116, 135, 941; **D9**: 067; **D10**: 033, 036, 137; **D11**: 037; **D12**: 009, 068, 072, 114, 123, 141, 153; **D13**: 016] Further information regarding the ADNI dataset can be found at <https://adni.loni.usc.edu/>.

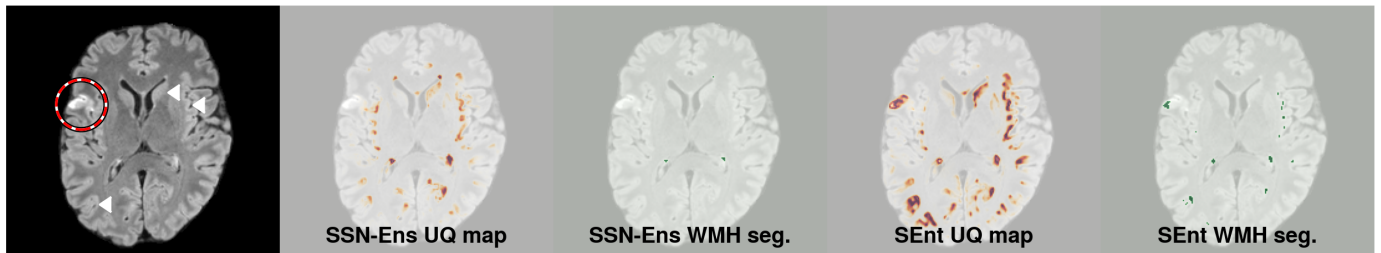
Appendix E. Further Qualitative Analysis - MSS3 images



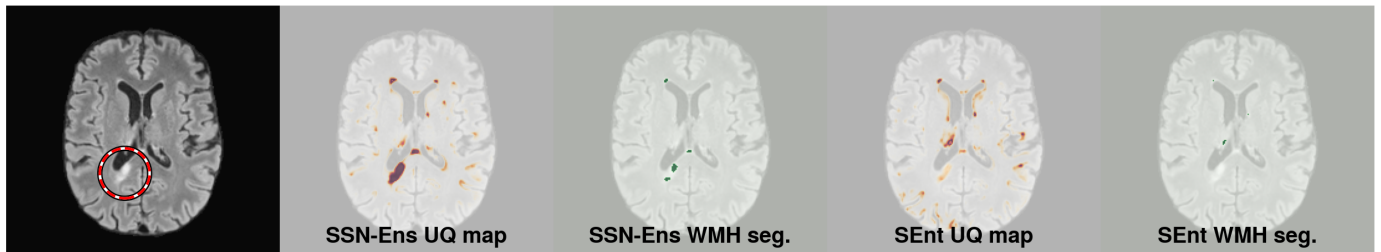
(a) **Incorrect segmentation of the insular cortex on OOD data.** In the right hemisphere the gray matter of the insular cortex is segmented by the SEnt model. White arrow points to a region in the insular cortex segmented as uncertain. The SSN-Ens model is clearly more robust, with less gray matter highlighted as uncertain, and none segmented in this case. The baseline SEnt model does not identify the centre of all segmented regions of the insular cortex as uncertain (see white arrow), demonstrating that the SEnt method does not produce semantically meaningful uncertainty maps on OOD data. Given that this tissue is gray matter, it is not within the aleatoric uncertainty of WMH and reflects the epistemic uncertainty of the model. However, an ideal model would neither segment this area nor deem it uncertain.



(b) **Small stroke lesions within the spatial distribution of WMH can be misidentified.** Here a small stroke lesion is segmented and not determined as uncertain (except for the boundary) for both models. This stroke lesion is within the distribution of plausible WMH, and if an annotator received no other information than the FLAIR image, may choose to annotate it as WMH (depending on the annotation policy).

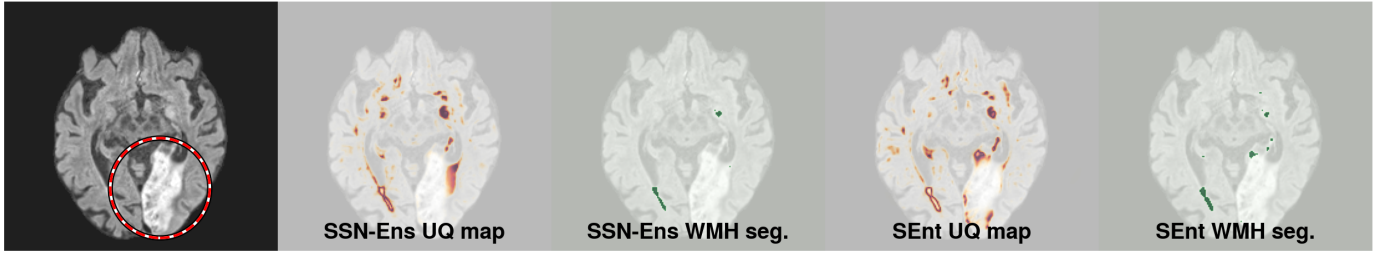


(c) **Difficulty with stroke lesion identification and nuisance gray matter identification for the SEnt model.** The SEnt model highlights part of the stroke lesion as uncertain. However, concerning, the part of the stroke lesion that is segmented as WMH is not uncertain. The SSN-Ens model does not segment this stroke lesion, nor is it uncertain unlike in other examples. This is most likely due to the stroke lesion appearing outside the typical spatial region of WMH. Both models identify parts of the gray matter, particularly in the insular cortex, as uncertain. The SEnt model further identifies substantial areas of the caudate nucleus (top arrow), insular cortex (middle arrow) and giri (bottom arrow) gray matter regions, as uncertain. This is nuisance information for a human to assess as it is clearly not WMH and limits the utility of uncertainty volumes in downstream tasks. The SSN-Ens model identifies less regions, and with lower intensity, as uncertain, making the uncertainty map easier to threshold (to remove low level uncertainty regions) and leaves less regions to be manually checked by a clinician.



(d) **SSN-Ens identifies a stroke lesion as uncertain.** Here a stroke lesion extends from the ventricles. Both models provide useful outputs here, SEnt (correctly) does not segment this as WMH while SSN-Ens identifies the whole region as highly uncertain, useful for identifying the stroke lesion in the image, albeit at the cost of partially segmenting the region.

Figure (E.1) Qualitative Analysis in the MSS3 dataset (Part 1). Visual assessment of the segmentations and UQ maps of the proposed SSN-Ens and baseline SEnt model. Rings denote definite stroke lesions.



(a) **Separate stroke lesion labels are required for stroke lesions outside the spatial distribution of WMH.** In this figure a large stroke lesion is presented. Due to its size, apparent texture in the image and location, this large hyperintense region is obviously not WMH. Consequently, neither model segments the stroke lesion or identifies it as uncertain. Hence, while the SSN-Ens model in other examples is effective at identifying stroke lesions, these must be at least partially within the spatial distribution of WMH. An effective model for quantifying the uncertainty in both stroke lesions and WMH pathologies must include stroke lesion labels during training. In this example SEnt partially (erroneously) segments the lesion, while SSN-Ens provides a valid segmentation.

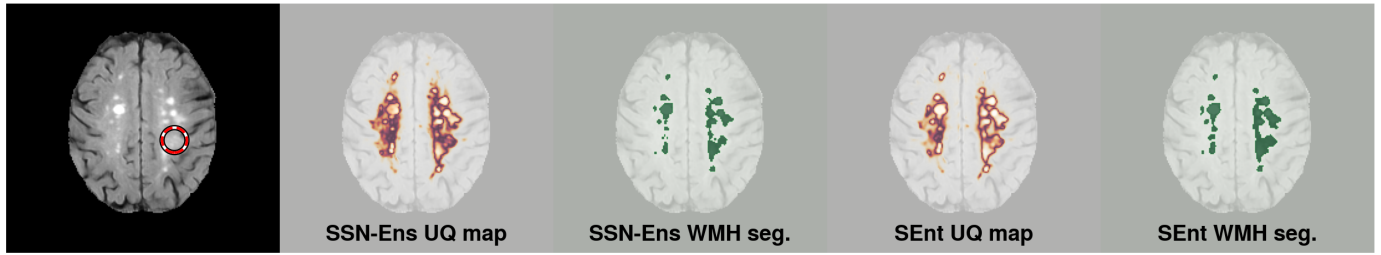


(b) **SSN-Ens identifies a stroke lesion as uncertain, while SEnt does not produce meaningful output.** Both methods segment parts of the stroke lesion as WMH incorrectly, although SSN-Ens only segments a small region, while identifying all of the hyperintense tissue as uncertain. However, the SEnt model only identifies the boundary of the hyperintense region stroke lesion as certain, and is confident that the lesion itself is a WMH. Concerningly, the cavitation within the stroke lesion is uncertain in the SEnt when this could never be a WMH. The SSN-Ens model correctly identifies only the hyperintense area as (highly) uncertain, making the stroke lesion easy to detect from the UQ map.



(c) **SEnt fails to identify a stroke lesion (segmented as WMH) as uncertain.** Here both models segment the majority of the stroke lesion as WMH. However, the SSN-Ens model identifies the entire stroke lesion as uncertain while SEnt does not. This allows the SSN-Ens UQ map to be used in a cluster-wise manner, easily identifying regions of the image that may or may not be WMH or stroke lesion. The SEnt UQ map mostly highlights the boundary of the segmented region as uncertain only, which does not tell us whether or not the entire region is possibly a stroke lesion and reduces the utility of the UQ map.

Figure (E.2) Qualitative Analysis in the MSS3 dataset (Part 2). Visual assessment of the segmentations and UQ maps of the proposed SSN-Ens and baseline SEnt model. Rings denote definite stroke lesions.



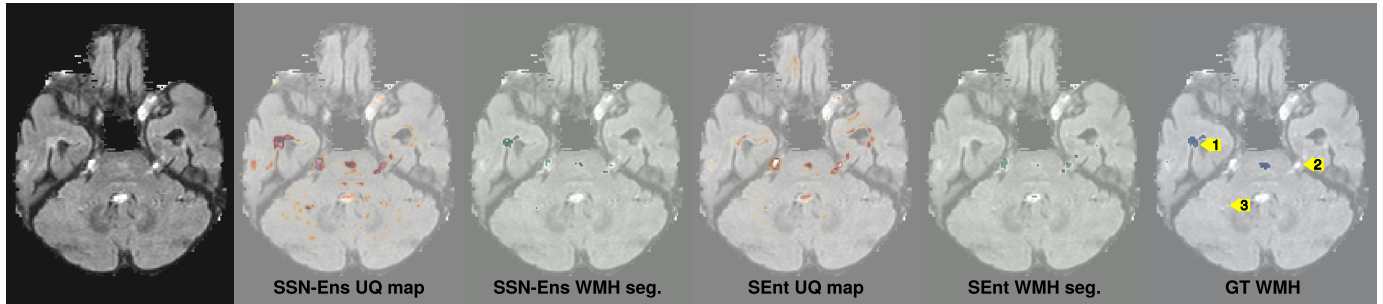
(a) **SSN-Ens uncertain for subtle stroke lesion.** In this image, a subtle stroke lesion, manually detected from a DWI scan, is present in the image. Only SSN-Ens is uncertain about this lesions, while SEnt only highlights the boundary as uncertain.



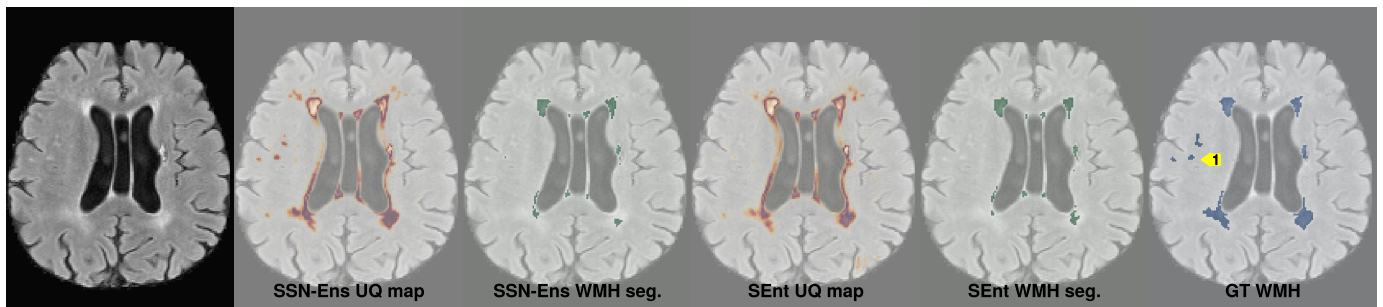
(b) **SEnt incorrectly segments a stroke lesion.** Here SEnt segments a stroke lesion and fails to identify the stroke lesion as uncertain. However, SSN-Ens successfully avoids segmenting the stroke lesion as WMH, while identifying the region as uncertain, making the lesion boundary easily identifiable from the UQ image. However, both models do not detect the stroke lesion at the bottom of the image in the UQ map, likely because this is not within the spatial distribution of WMH.

Figure (E.3) Qualitative Analysis in the MSS3 dataset (Part 3). Visual assessment of the segmentations and UQ maps of the proposed SSN-Ens and baseline SEnt model. Rings denote definite stroke lesions. White arrows point to gray matter regions highlighted as uncertain. Not all such gray matter regions are marked.

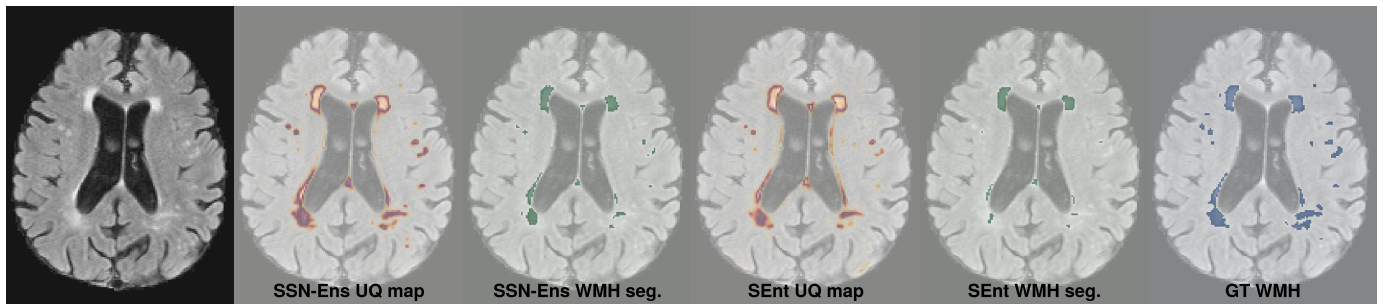
Appendix F. Further Qualitative Analysis - Small Lesions in the Challenge Dataset



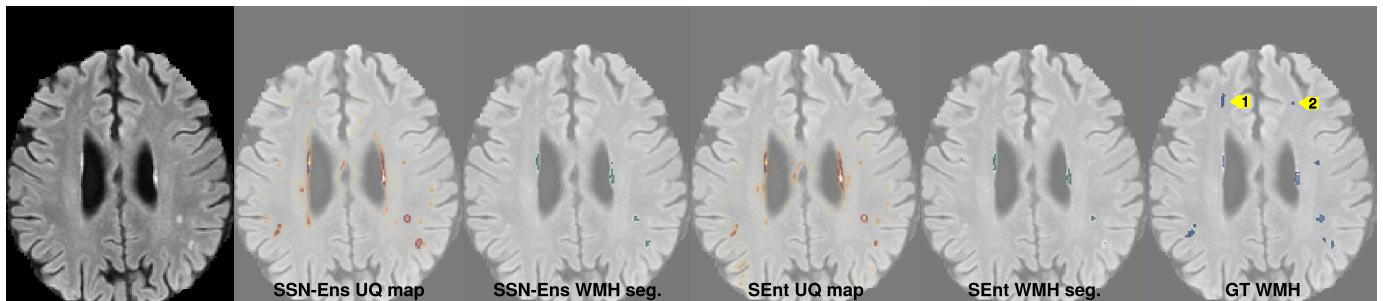
(a) **Arrow 1:** SEnt baseline model fails to segment this WMH, and fails to detect the region as uncertain. **Arrow 2:** Both models introduce false positive WMH here, but SEnt only highlights the boundary of the lesion as uncertain, while SSN-Ens identifies the entire segmented region as uncertain. **Arrow 3:** SSN-Ens model typically introduces regions of the cerebellar hemisphere as uncertain, meaning that low signal in the UQ map should be filtered out prior to visual assessment.



(b) **Arrow 1:** A cluster of 3 WMH of which SEnt fails to segment all 3 while SSN-Ens partially segments a single WMH instance. In the SSN-Ens UQ map all three are detected with high coverage, however SEnt yields very low to zero signal in the UQ map.

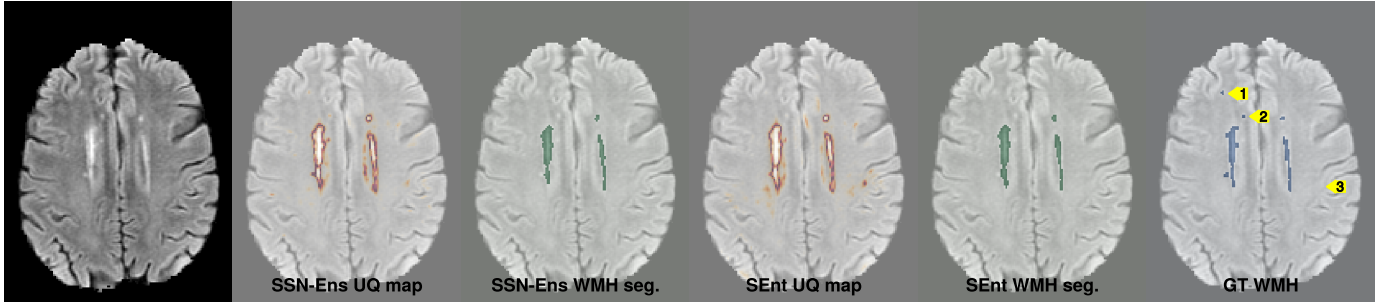


(c) Both methods fail to segment a number of small WMH in this example. However, the UQ map for both methods highlights almost all small WMH. The SSN-Ens yields higher signal in the UQ map for false negatives across the image compared to regions that are not WMH, i.e. the uncertainty map is better calibrated.

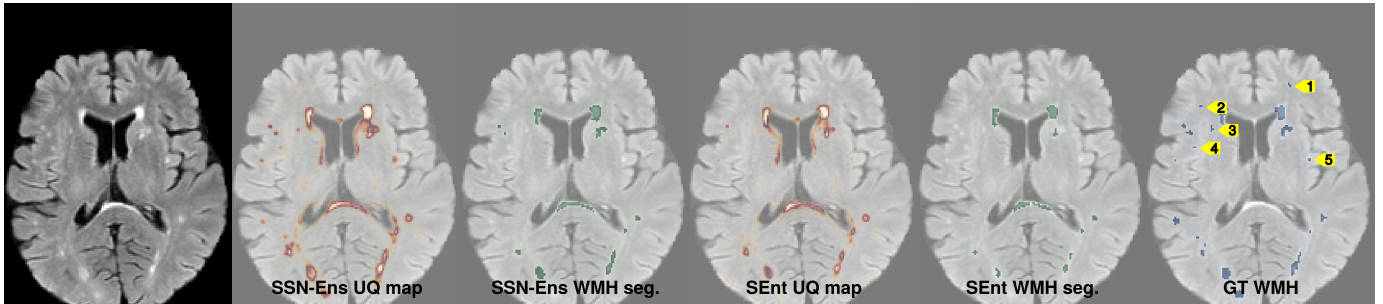


(d) **Arrow 1:** A small WMH is partially detected in the UQ map by SSN-Ens with low signal. SEnt does not identify any part of this WMH as uncertain. **Arrow 2:** Both methods silently fail to either segment this WMH or identify it as uncertain.

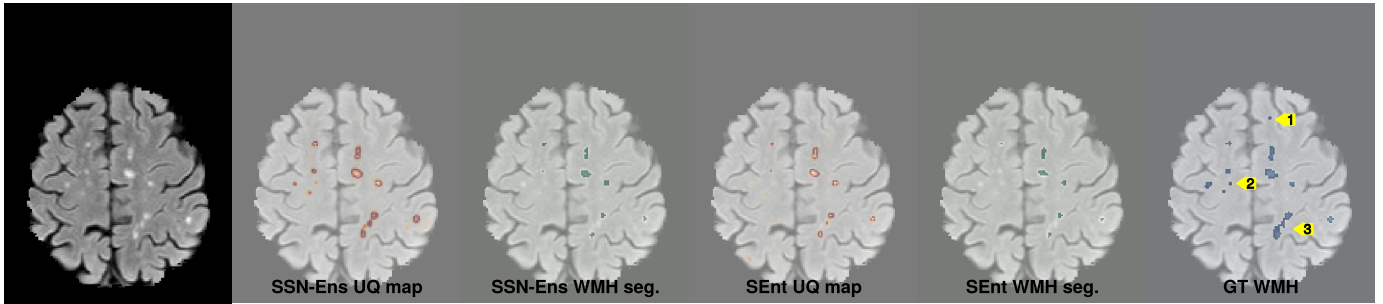
Figure (F.1) Qualitative Analysis in the Challenge dataset (part 1).



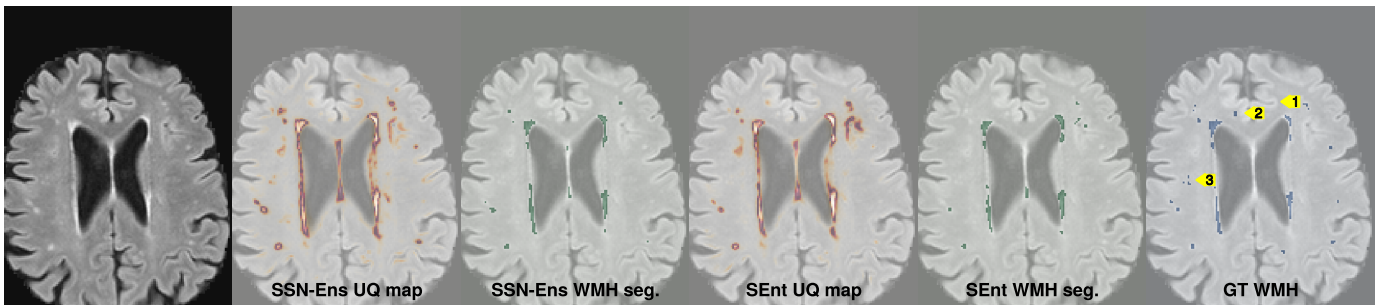
(a) **Arrow 1:** both methods fail to segment this small lesion. SSN-Ens highlights, with very low signal intensity, a few voxels in the centre of the WMH. **Arrow 2:** A repeat of **Arrow 1**. **Arrow 3:** Both methods highlight areas in the uncertainty map that appear to reflect textural changes and gray matter regions in the image, not hyperintensities. While both methods (incorrectly) find a potential WMH at this location, SSN-Ens shows lower signal intensity in the UQ map, demonstrating improved calibration in the uncertainty map.



(b) **Arrow 1:** Small WMH is unsegmented by both methods, but detected in the UQ map of SSN-Ens. **Arrow 2, Arrow 3, Arrow 4:** Repeat of **Arrow 1**. **Arrow 5:** A small WMH, unsegmented by both models. SSN-Ens finds the entire WMH highly uncertain, while SEnt find the WMH partially uncertain, with lower signal intensity in the WMH map.



(c) **Arrow 1:** both methods fail to segment this small lesion. SSN-Ens highlights, with very low signal intensity, a few voxels in the centre of the WMH. **Arrow 2:** Small WMH is unsegmented by both methods, but detected in the UQ map of SSN-Ens. **Arrow 3:** Both methods partially segment this cluster of WMH, however SEnt fails to identify as uncertain the regions of the cluster that remain unsegmented.



(d) **Arrow 1:** SSN-Ens introduces a number of areas of gray matter as uncertain in the image. This makes segmenting the uncertainty map less useful, as a higher threshold must be set to filter out nuisance regions from the image. This is an effect of domain shift due to MRI acquisition parameter change. In the Challenge dataset, only images collected from the AMS institute (see D.1) with the 3T Philips Ingenuity Scanner exhibit this effect. **Arrow 2:** Both methods fail to identify this WMH in either the segmentation or UQ map. **Arrow 3:** A cluster of 3 small WMH are identified as uncertainty in the SSN-Ens UQ map only. Similarly in the right hand hemisphere, there are three small WMH; only SSN-Ens clearly identifies the top and bottom WMH in the uncertainty map, while neither clearly detect the middle WMH.

Figure (F.2) Qualitative Analysis in the Challenge dataset (part 2).

Appendix G. Further Fazekas Classification types

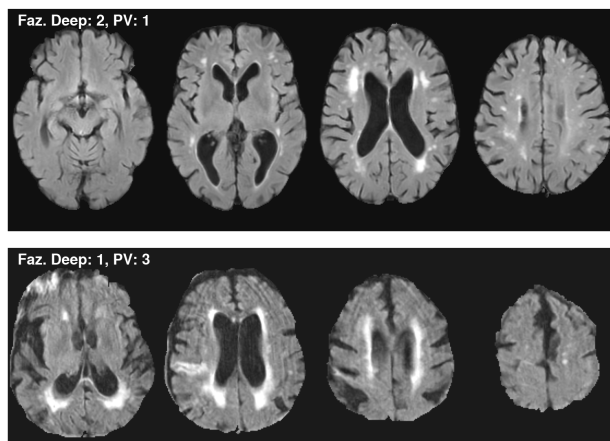


Figure (G.1) Fazekas Categories shown where Deep WMH \neq PV WMH. Examples taken from the CVD dataset.

Appendix H. Fazekas Classification Results per heldout dataset

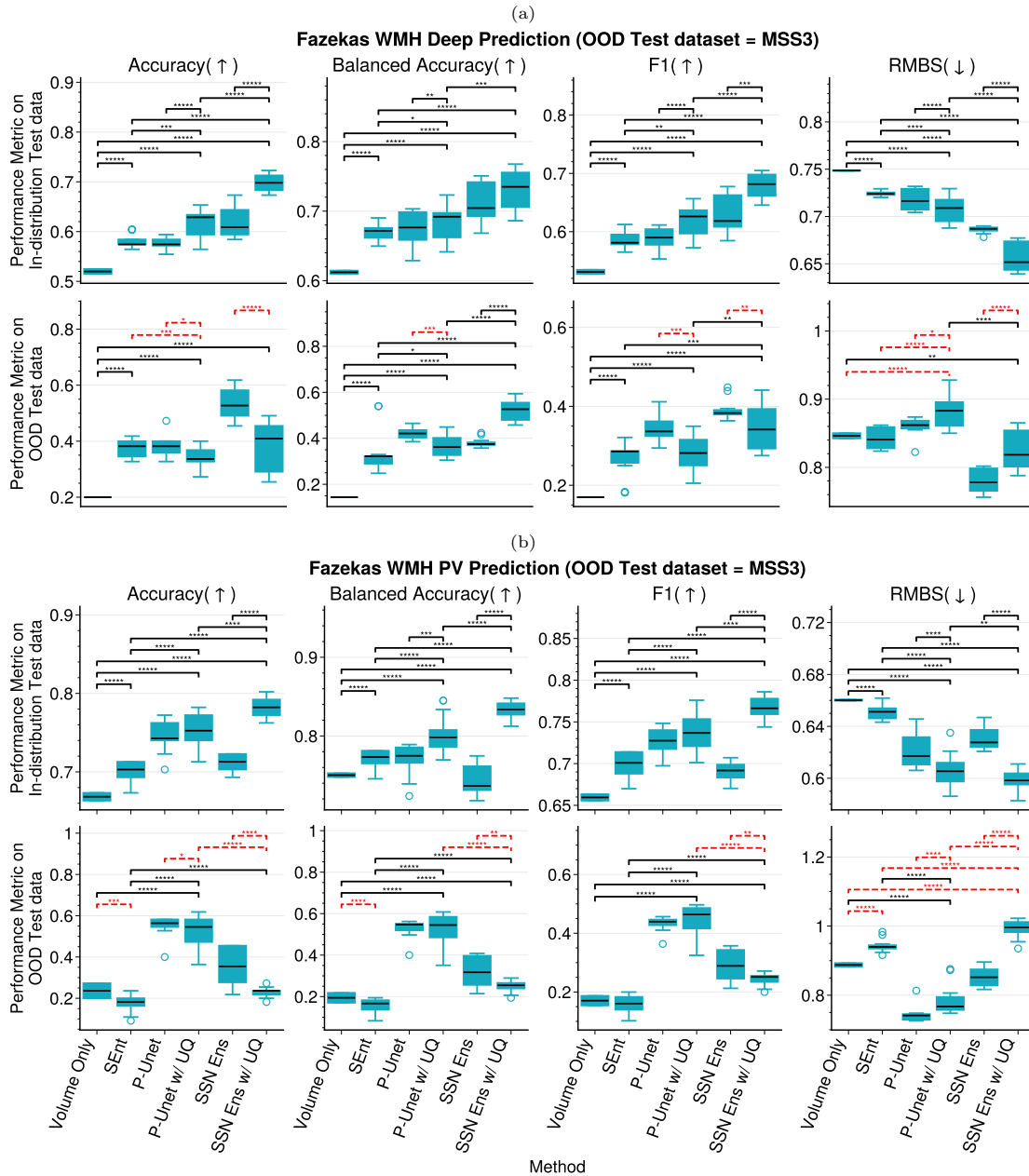


Figure (H.1) Distribution of Fazekas prediction scores for (a) the Deep and (b) PV WMH prediction task with the MSS3 dataset used as an OOD holdout. Pairwise two-tailed t-test between each set of method hyperparameter configurations as per Figure 7 shown with the number of * denoting $p < 0.05/0.01/0.001/0.0001/0.00001$. Black (dotted red) line/* if the right (left) hand model significantly improves the score over the left (right) hand model. All significant pairwise relationship between methods are stated.

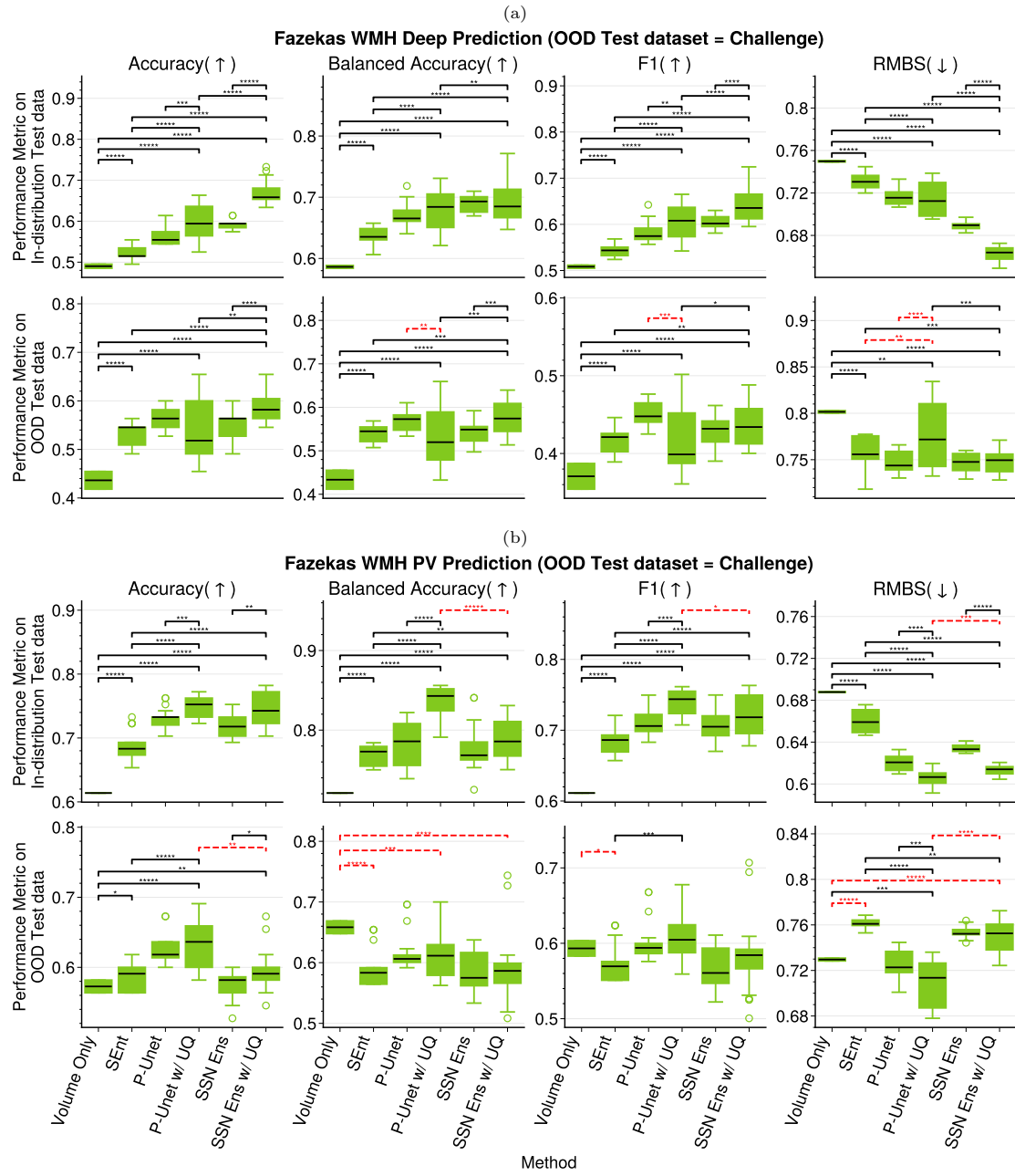


Figure (H.2) Distribution of Fazekas prediction scores for (a) the Deep and (b) PV WMH prediction task with the Challenge dataset used as an OOD holdout. Pairwise two-tailed t-test between each set of method hyperparameter configurations as per Figure 7 shown with the number of * denoting $p < 0.05/0.01/0.001/0.0001/0.00001$. Black (dotted red) line/* if the right (left) hand model significantly improves the score over the left (right) hand model. All significant pairwise relationship between methods are stated.

Appendix I. Analyst volume policy impacts Fazekas classification performance

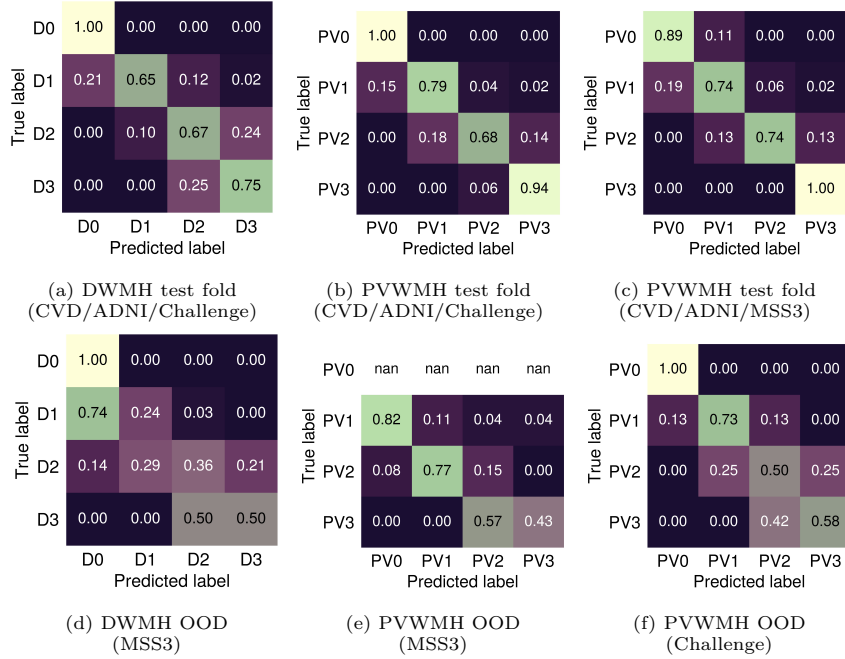


Figure (I.1) Confusion matrices showing performance of SSN-Ens w/ UQ features on in-distribution and OOD testing data. For the purposes of comparison, the model hyperparameters that yield the highest balanced accuracy score on the in distribution test data are used. (a-c): Confusion matrix for the in-distribution test fold. (d-f): Corresponding confusion matrix for the OOD testing data from the row above. E.g (a) shows the DWMH results when CVD, ADNI and Challenge are used for the in distribution train/test split while (d) shows the corresponding OOD results using the MSS3 dataset.

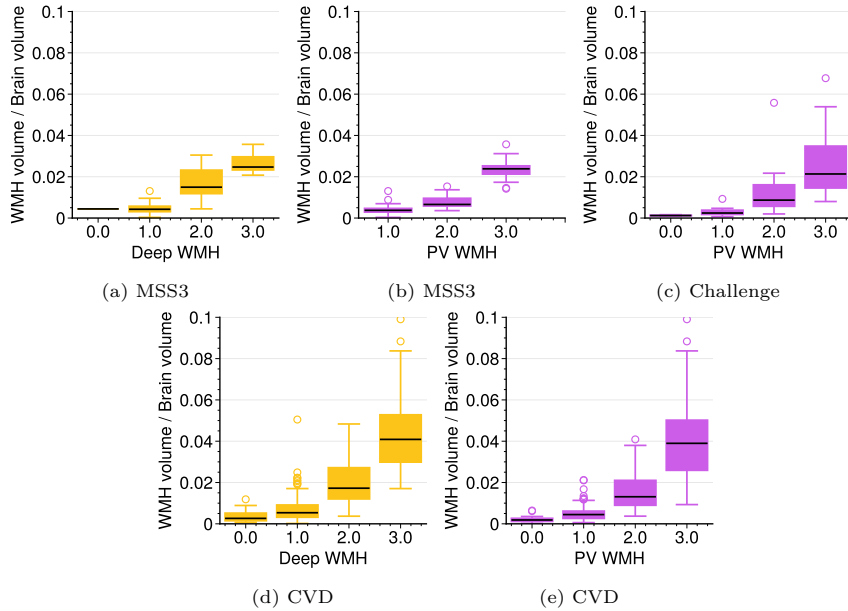


Figure (I.2) Distribution of WMH volume as a proportion of Brain volume for each Fazekas class. (a) DWMH on the MSS3 dataset. (b) PVWMH on the MSS3 dataset. (c) PVWMH on the Challenge dataset. (d) DWMH on the CVD dataset. (e) PVWMH on the CVD dataset.